Quaternary Science Reviews 195 (2018) 133–152

Contents lists available at ScienceDirect

Quaternary Science Reviews

journal homepage: www.elsevier.com/locate/quascirev

Paleoceanography of northeastern Fram Strait since the last glacial maximum: Palynological evidence of large amplitude changes

Jade Falardeau [a, *], Anne de Vernal [a], Robert F. Spielhagen [b, c]

[a] GEOTOP-UQAM, CP 8888 Montréal, H3C 3P8, Canada
[b] GEOMAR Helmholtz Centre for Ocean Research, 24148 Kiel, Germany
[c] Academy of Sciences, Humanities and Literature, 55131 Mainz, Germany

ARTICLE INFO

Article history:
Received 11 May 2017
Received in revised form
31 May 2018
Accepted 30 June 2018
Available online 19 July 2018

Keywords:
Fram strait
Last glacial maximum (LGM)
Late and post-glacial
Holocene
Temperature
Salinity
Sea ice
Dinocysts

ABSTRACT

Sea-surface conditions in northeastern Fram Strait since the last glacial maximum (LGM) were reconstructed from cores MSM5/5-712-2 and PS2863/1–2 based on palynological assemblages, ecological preferences of dinocysts and application of the modern analog technique. Dinocyst in LGM sediments are sparse, but their assemblages reflect mild summer conditions. Given the regional context and evidence from other tracers, the dinocyst assemblages of the LGM could relate to regional fluxes of dinocysts during exceptional mild summers. From 19 to 14.7 ka, dinocyst data suggest very cold conditions with extensive sea-ice cover, while abundant reworked palynomorphs indicate intense glacial erosion. An abrupt transition at 14.7–14.5 ka was marked by a peak in summer temperatures coinciding with a rapidly deposited sediment layer related to a regional meltwater plume event in western Svalbard. From 14.7 to 12.6 ka, large seasonal temperature contrasts with mild summers and cold winters together with low salinity indicate continuous melting of the Svalbard Barents Sea ice sheet fostered by warm climate. At 12.6 ka, the regional onset of the Younger Dryas was marked by cooling and increased salinity. On a regional scale, the 12.6–12 ka interval corresponds to an important transition involving enhanced circulation of Arctic waters around Svalbard and establishment of coastal fronts along its northern and western margins. Modern-like oceanic conditions with relatively high salinity and low seasonal temperature contrast developed at about 7.6 ka. Since then, a slight cooling is observed, especially in winter. This study offers a comprehensive picture of the deglacial phases in eastern Fram Strait with unique data on the sea-surface salinity, which controls surface water stratification and plays an important role in ocean circulation.

1. Introduction

The Norwegian Atlantic Current and its northernmost derivatives reach the Arctic Ocean notably through the Fram Strait, which is the main gateway between the Atlantic and the Arctic oceans (Fahrbach et al., 2001; Maslowski et al., 2004; Schauer, 2004). Hence, these currents are an important heat source to the Arctic Ocean shaping the northern limit of the regional sea-ice margins, which in turn plays an important role for the energy budget at the Earth's surface. Furthermore, as the Atlantic Water (AW) flows northward in eastern Fram Strait, heat loss to the atmosphere accompanied with surface water cooling leads to increased density of surface waters, thus potentially contributing to both the strength of the Atlantic Meridional Overturning Circulation (AMOC) and the rate of North Atlantic Deep Water (NADW) formation. Therefore, the oceanography of the Fram Strait is critical not only for the climate in the Arctic realm but also for the global thermohaline circulation. In this context, the objective of the present study is to document changes in sea-surface conditions in the northeastern Fram Strait since the last glacial maximum (LGM; 23–19 ka; Kucera et al., 2005) to assess the role of northward heat flux from AW advection on deglaciation and climate variations during the postglacial.

Many studies have investigated the changes in AW inflows in Fram Strait during the LGM and the deglaciation. Most of them are based on planktic and/or benthic foraminifer assemblages and stable isotope analyses of foraminifer shells (cf. Hebbeln et al., 1994; Sarnthein et al., 1995, 2003; Nørgaard-Pedersen et al., 2003; Hald

* Corresponding author.
E-mail address: falardeau.jade@courrier.uqam.ca (J. Falardeau).

https://doi.org/10.1016/j.quascirev.2018.06.030
0277-3791/

et al., 2001, 2007; Ślubowska-Woldengen et al., 2007, 2008; Rasmussen et al., 2007, 2012; Werner et al., 2011, 2013; 2016; Aagaard-Sørensen et al., 2014a,b, Chauhan et al., 2014; Zamelczyck et al., 2014; Bartels et al., 2017; Consolaro et al., 2018). Other studies are based on sedimentological data (Andersen et al., 1996; Forwick and Vorren, 2009; Jessen et al., 2010). However, as most of these studies document paleoceanographical conditions in sub-surface and bottom waters, there is still little information on the surface water conditions. To date, reconstructions of past sea-surface conditions mostly document sea-ice cover using the organic biomarker IP_{25} (Müller et al., 2012; Müller and Stein, 2014; Bartels et al., 2017) and sea-surface temperature estimated from alkenones during the LGM (Rosell-Melé and Comes, 1999) and the Early Holocene (Calvo et al., 2002; Marchal et al., 2002; Risebrobakken et al., 2011). Data documenting variations of seasonal temperatures and sea-surface salinity off western Svalbard since the LGM remain rare.

Here we present two new dinoflagellate cyst (or dinocyst) records from northeastern Fram Strait covering the last 23,000 years. The data were used to apply the modern analog technique for quantitative reconstruction of several sea-surface parameters, including winter and summer sea-surface temperatures (SSTs) and sea-surface salinities (SSSs), along with sea-ice cover extent (month/yr) and productivity (gC/cm^2yr), simultaneously. Hence, our data provide information on freshwater inputs from glaciers and seasonal gradients of temperatures (Rochon et al., 1999; de Vernal et al., 2001, 2005; 2013; Grøsfjeld et al., 2009), which are critical parameters in ice-ocean dynamics, especially during phases of ice retreat. Core sites MSM5/5–712 and PS2863 are located on the western and northwestern continental slopes of Svalbard (Fig. 1; Table 1). Previous studies from site MSM5/5–712 (Spielhagen et al., 2011; Werner et al., 2013; Aagaard-Sørensen et al., 2014a; Zamelczyk et al., 2014) have provided a stratigraphic framework with multidecadal temporal resolution in which biomarkers and stable isotopes have illustrated qualitative changes of the AW inflow and sea-ice cover extent (Werner et al., 2011, 2013; Müller et al., 2012; Müller and Stein, 2014; Spielhagen et al., 2014; Zamelczyk et al., 2014). In addition to developing a more detailed portrait of the surface water conditions from the LGM to present, our study of the two above mentioned sites aims at contributing to a better understanding of the AW modifications along its pathway, from the relatively confined channel of the eastern Fram Strait to the open Arctic Ocean north of Svalbard, where strong ocean-atmosphere heat transfer presently occurs.

2. Regional hydrography

There are two main currents in the Fram Strait (Fig. 1; Fahrbach et al., 2001; Schauer, 2004; Rudels et al., 2005; Schauer et al., 2008). In the west, the East Greenland Current (EGC) flows southward and transports cold and fresh waters from the Arctic Ocean, thus playing a major role in iceberg and sea-ice export to the North Atlantic. In the east, the West Spitsbergen Current (WSC) circulates northward along the western continental slope of Svalbard and carries relatively warm and saline Atlantic waters towards the Arctic Ocean. It originates from two distinct branches in the Nordic Seas: the Norwegian Atlantic Slope Current (NwASC) and the Norwegian Atlantic Current (NwAC), further named the WSC western branch. Parts of the NwASC turns east at the surface into the shallow Barents Sea (Rudels et al., 1999), where it is responsible for significant heat transport (5.07 Sv; 106 TW; Maslowski et al., 2004) while the rest of the water masses continues north as the WSC core. Parts of the WSC western branch bifurcate to the west without extending further than 80–81°N (Rudels et al., 2000) through the Return Atlantic Current (RAC) following topographical features, to finally turn south with the EGC (Gascard et al., 1995). The two main branches converge into the WSC core around 78°N due to the bottom topography (Walczowski and Piechura, 2007).

Because of the complex bathymetry of the Fram Strait, the WSC core splits into three branches (Manley, 1995): a western branch (RAC), a central branch called the Yermak Branch (YB), which flows north and reaches the Arctic Ocean along the western and northern shelf of the Yermak Plateau (YP), and the Svalbard Branch (SB). This branch flows east following the northern Svalbard shelf and continues by circulating south of the Yermak Plateau.

Arctic waters circulate southward through the East Spitsbergen Current (ESC) and follow the east Svalbard coast in the Barents Sea (Loeng, 1991). The ESC is renamed as the South Cape Current (SCC) after passing the Storfjorden, in south Svalbard, and follows the western coast of Svalbard carrying freshwater from glaciers melt and river runoff in summer (Skogseth et al., 2005).

The WSC transports about 11.6 Sv at 78°50′N corresponding to 70.6 TW of heat (Walczowski et al., 2005). Previous studies from moored instruments obtained similar values with mean annual transport of 9 ± 2 to 10 ± 1 Sv (Schauer, 2004) and a monthly mean average of 9.5 ± 1.4 Sv (Fahrbach et al., 2001). The regional sea-ice cover extent is mainly controlled by the advection of warm AW. Site MSM5/5–712 is located under the path of the WSC on the western continental slope of Svalbard and it is therefore largely influenced by AW. Site PS2863 is located 200 km north of MSM5/5–712 downstream of the WSC and is thus under distal influence of AW and close to the limit of mean sea-ice extent in summer which corresponds to the Polar Front.

At site PS2863, the mean sea-surface temperature and salinity in summer are 2.3 ± 2.3 °C and 33.3 ± 0.9 psu, respectively (1900–2001 data from the World Ocean Atlas, 2001; Conkright et al., 2002, Table 1). The sea-ice cover is highly variable at the core site since it is located close to the sea-ice margin. Hence, the sea-ice cover with concentration >50% varied between 0 and 11 months/yr from 1954 to 2003, with an average of 3.7 ± 3.2 months/yr (data provided by the NSIDC in Boulder). At site MSM5/5–712, the mean-sea surface temperature and salinity in summer are 4.9 ± 1.4 °C and 34.73 ± 0.43 psu, respectively (Conkright et al., 2002, Table 1). Sea-ice cover with concentration >50% varied between 0 and 6 months/yr from 1954 to 2003, with an average of 1.2 ± 1.7 months/yr (data from NSIDC, 2003).

3. Methods

Gravity core PS2863-1 (80°33.46′N, 10°17.96′E; water depth 808 m) was collected in 1997 during the *RV Polarstern* expedition ARK-XIII/2 (Stein and Fahl, 1997). The core is 580 cm long. The uppermost 184 cm were subsampled at 4 cm intervals for palynological analyses. Box core PS2863-2 from the same location is 41 cm long. It was subsampled at a 1 cm interval (Table 1). The results from the two cores were combined into a composite record referred to as PS2863 (see detailed counts of palynomorphs in Falardeau, 2017).

Sediment core MSM5/5-712-2 (78°54.94′N, 6°46.04′E; water depth 1487 m) was retrieved from *RV Maria S. Merian* in 2007 (Budéus, 2007). The kastenlot core has a total length of 950 cm. Palynological results from this core (hereafter MSM5-712) are presented at 4 cm intervals for the uppermost 283 cm and at 8 cm intervals down to 777 cm (Table 1).

Samples were prepared for palynological analyses in the micropaleontology laboratory of GEOTOP according to standard procedures (de Vernal et al., 2010). In short, approximately 5 cm^3 of sediment were wet sieved at 10 and 106 μm after measurement of their volume and their weight (wet and dry). One capsule of *Lycopodium clavatum* with a known number of spores was added for further palynomorph concentration calculations (Matthews, 1969). The 10–106 μm fraction was treated with hydrochloric acid

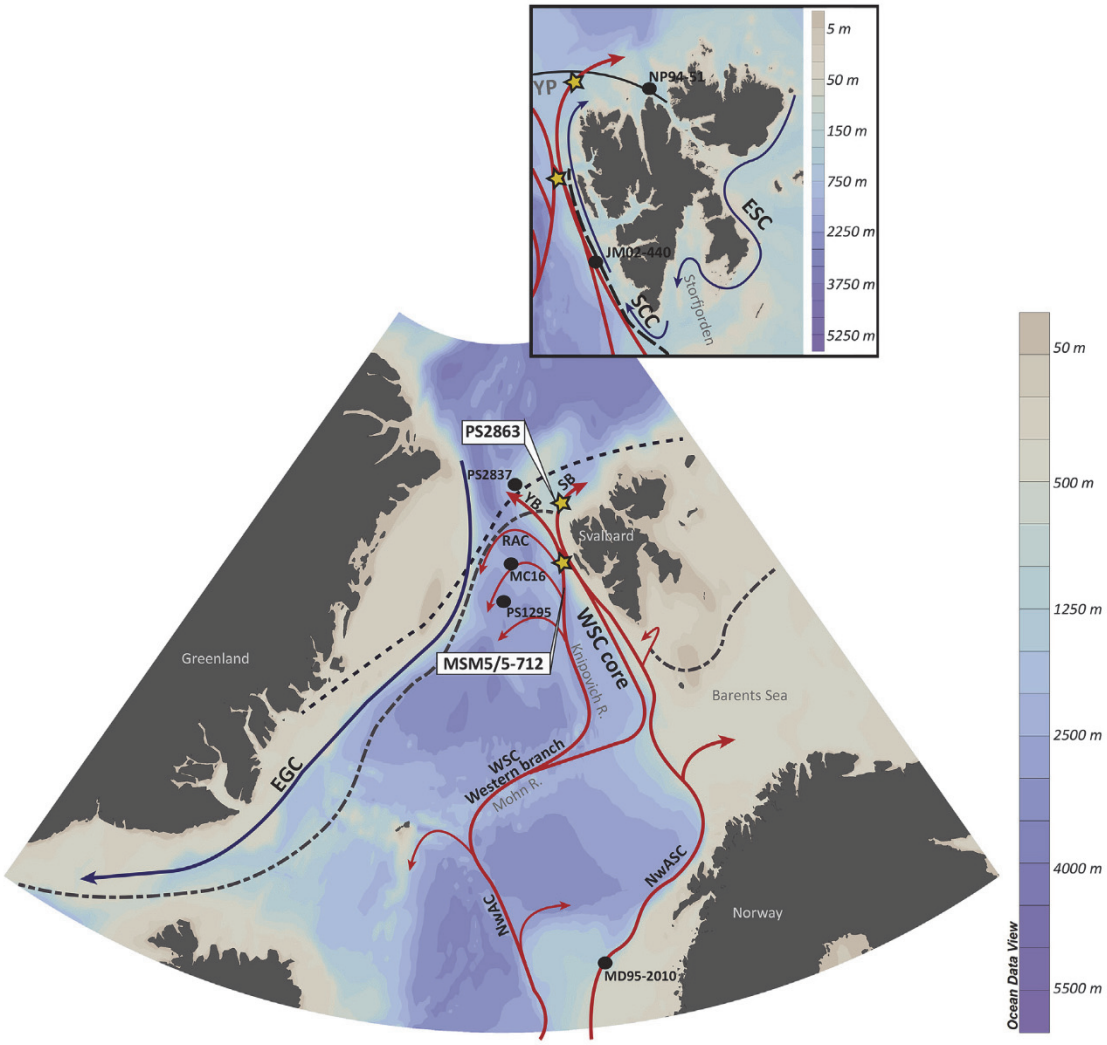

Fig. 1. Map of the main surface currents in the Fram Strait and around Svalbard and location of the study sites MSM5/5–712 and PS2863 (yellow stars). Limits of minimum (September) and maximum (March) median sea-ice cover extent from 1979 to 2016 obtained from the Sea Ice Index of the National Snow and Ice Data Center (NSIDC; cf. Fetterer et al., 2016) are represented by blue and gray dotted lines, respectively. Red arrows indicate warmer Atlantic waters derived from the North Atlantic Drift and were reproduced with respect to Walczowski et al. (2005). Blue arrows indicate cold surface water currents. In the Svalbard close-up, the Arctic Coastal Front and the Polar Front are depicted, shown by a dotted and a uniform black line, respectively. Locations of other cores discussed in the text are indicated by black dots. Main features of the sea-floor such as the Yermak Plateau (YP), the Storfjorden and the Mohn and Knipovich ridges are also indicated on the map. EGC: East Greenland Current, WSC: West Spitsbergen Current, NwASC: Norwegian Atlantic Slope Current, NwAC: Norwegian Atlantic Current, ESC: East Spitsbergen Current, SCC: South Cape Current, RAC: Return Atlantic Current, SB: Svalbard Branch, YB: Yermak Branch. (For interpretation of the references to color in this figure legend, the reader is referred to the Web version of this article.)

Table 1
Information on the study cores.

Core name	Abbreviation used in text	Core location	Latitude	Longitude	Water depth (m)	Core length (cm)	Modern sea-surface conditions			Core sampling	
							SST in summer (°C)	SSS in summer (psu)	Sea-ice cover (month/yr)	Length (cm)	Interval (cm)
MSM5/5-712-2	MSM5-712	Western Svalbard margin	78°54.937′N	06°46.036′E	1487	950	4.94 ± 1.40	34.73 ± 0.43	1.2 ± 1.7	10–283 283–777	4 8
PS2863-1 PS2863-2	PS2863	NW Svalbard margin	80°33.46′N 80°33.47′N	10°17.96′E 10°17.93′E	808 807	580 41	2.3 ± 2.3	33.3 ± 0.9	9.32 ± 2.0	41–184 0–39	4 1

Core location, water depth (m) and recovery (cm); present day sea-surface conditions at the core sites (Conkright et al., 2002) and sea-ice cover from NSIDC. Sections and subsampling intervals (cm) are indicated.

(HCl 10%) and hydrofluoric acid (HF 49%) to dissolve carbonate and silica particles, respectively. Residues were mounted on slides in glycerin jelly for microscopic analysis.

Dinocyst and other palynomorph concentrations were calculated as follows:

$$Np = (Ne \times np)/ne$$

where Np is the total number of dinocysts in the sample, Ne is the known number of *L. clavatum* spores in the capsule added to the

sample, np is the number of dinocysts counted and ne is the number of *L. clavatum* counted. The total number of dinocysts was used to calculate dinocyst concentrations as follows:

$$Np/dry\ sediment\ weight\ (g) = Dinocyst\ concentrations\ (\#/g)$$

or:

$$Np/volume\ \left(cm^3\right) = Dinocyst\ concentrations\ \left(\#/cm^3\right)$$

The total uncertainty of calculated concentration was determined from the equation of Stockmarr (1971), which is based on the standard deviation of number of spores in the *L. clavatum* capsules, the error on the number of cysts counted and number of *L. clavatum* spores counted. The total error never exceeded 22%.

The results from the latter calculation for dinocyst concentrations was used to determine the fluxes:

$$Sedimentation\ rate\ (cm/yr) \times Concentration\ \left(\#/cm^3\right) = Flux\ \left(\#/cm^2/yr\right)$$

The sedimentation rate was calculated from a linear interpolation between each sample based on the established age vs. depth relationship (see text section 4, Fig. 2).

Analysis of the palynological content includes dinoflagellate cysts, foraminiferal organic linings, the freshwater chlorophyte *Pediastrum* and reworked pre-Quaternary palynomorphs. The foraminiferal linings, consisting of refractory organic matter, can be used as indirect tracers of productivity as benthic foraminifers depend upon organic matter fluxes (e.g., de Vernal et al., 1992; Leduc, 2001; Jorissen et al., 2007). Pollen grains, spores and other palynomorphs were also counted (see Falardeau, 2017), but not used here.

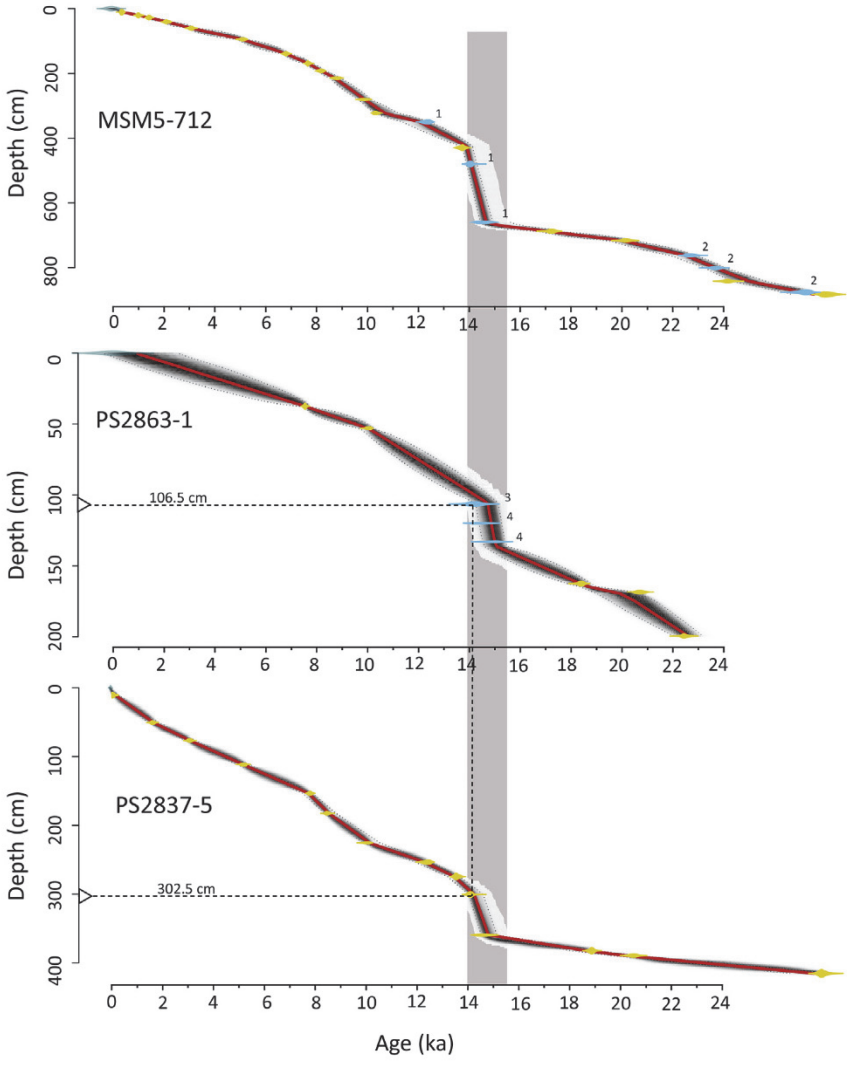

Fig. 2. Age model of cores MSM5-712, PS2863-1 and PS2837-5 obtained by using the Bacon 2.2 software (Blaauw and Christen, 2011) (see Table 2 for data and text section 4). The red line corresponds to the weighted average. Gray areas show the most probable ages based on Bayesian statistics with default probability intervals of 95% (2-sigma). The dates are indicated in yellow and the correlated tie points are indicated in blue, with numbering as follows: (1) correlations with core PS2837-5 based on total organic carbon (cf. Müller and Stein, 2014), (2) correlations with the western Svalbard magnetic susceptibility stack of Jessen et al. (2010) from Müller and Stein (2014), (3) sedimentological correlation with core PS2837-5 based on IRD (this study; see triangles and dotted lines), (4) correlation of a fine-grained layer in core PS2863-1 with the rapidly deposited layer in the western Svalbard (Jessen et al., 2010). The vertical shaded zone corresponds to the interval of the rapidly deposited sediment layer defined by Jessen et al. (2010), including its 95% probability. Since the rapid sedimentation rate event is well-documented regionally (Jessen et al., 2010; Lucchi et al., 2015), we added hiatuses at the depths of the first and last age of the event, so the model would interpret the accumulation rate of this interval separately. (For interpretation of the references to color in this figure legend, the reader is referred to the Web version of this article.)

Table 2
Radiocarbon chronology of cores MSM5-712, PS2863-1 and PS2837-5.

Core	Depth (cm)	Conventional ^{14}C age (^{14}C years BP)	Calibrated age (cal. years BP)	Minimum age	Maximum age	Lab n°	Reference
MSM5-712	10–12	815 ± 25	381.7	218	471.4	KIA 45217	Werner et al., 2013
MSM5-712	20–22	1570 ± 25	1018.7	884	1161.2	KIA 41024	Werner et al., 2013
MSM5-712	27–29	1985 ± 25	1432.2	1299.7	1568.6	KIA 45218	Werner et al., 2013
MSM5-712	40–42	2565 ± 25	2114.1	1935.9	2284	KIA 45219	Werner et al., 2013
MSM5-712	60.5	3365 ± 30	3093.8	2896	3295.1	SacA 19113	Giraudeau (in preparation)
MSM5-712	94.5	4915 ± 30	5077.5	4861.2	5264.5	SacA 19114	Giraudeau (in preparation)
MSM5-712	139	6440 ± 30	6796.2	6622.9	6960.5	SacA 19115	Giraudeau (in preparation)
MSM5-712	169	7305 ± 35	7669.5	7530.1	7809.3	KIA 38080	Werner et al., 2013
MSM5-712	192	7815 ± 45	8194.9	8029.8	8342.9	KIA 41025	Werner et al., 2013
MSM5-712	214.5	8362 ± 50	8730.4	8526.8	8937.4	Poz-30723	Aagaard-Sørensen et al., 2014a
MSM5-712	280.5	9220 ± 50	9895.3	9640.2	10,137.6	KIA 37423	Aagaard-Sørensen et al., 2014a
MSM5-712	322.5	9580 ± 47	10,699.2	10,324.1	11,203.5	Poz-30725	Aagaard-Sørensen et al., 2014a
MSM5-712	350	10,940 ± 50[a]	12,047.8	11,375.4	12,443.1	KIA 7571	Nørgaard-Pedersen et al., 2003
MSM5-712	428–431	12,358 ± 63	13,920.4	13,737.9	14,137.5	Poz-30726	Aagaard-Sørensen et al., 2014a
MSM5-712	480	12,655 ± 60[a]	14,077.5	13,892.8	14,296.8	KIA 7572	Nørgaard-Pedersen et al., 2003
MSM5-712	660	12,9400 ± 70[a]	14,792.5	14,450	15,620	KIA 10864	Nørgaard-Pedersen et al., 2003
MSM5-712	687.5	14,650 ± 75	17,052.9	16,555.4	17,465.1	Poz-30727	Zamelczyk et al., 2014
MSM5-712	716.25	17,200 ± 120	19,912.5	19,337.2	20,379.1	Poz-38427	Zamelczyk et al., 2014
MSM5-712	762.25	19,300 ± 140	22,444.5	21,856.3	22,841.4	Poz-30728	Zamelczyk et al., 2014
MSM5-712	801	20,150 ± 130[b]	23,669.9	23,237	24,059.6	–	Jessen et al., 2010
MSM5-712	842	20,580 ± 130[b]	24,972.2	24,285.4	25,628.1	–	Jessen et al., 2010
MSM5-712	876	23,340 ± 200[b]	27,068.9	26,339.5	27,562	–	Jessen et al., 2010
MSM5-712	882.75	24,480 ± 190	27,521.8	26,659.1	27,944.5	Poz-30729	Zamelczyk et al., 2014
PS2863-1	36–39	7150 ± 35	7537.3	7319	7,7717.3	OS-122305	This study
PS2863-1	52–54	9336 ± 40	10,156.1	9841.2	10,508.4	KIA-50537	This study
PS2863-1	120	12,840 ± 150[b]	14,700.4	14,250.5	15,122.9	–	Jessen et al., 2010
PS2863-1	133	13,140 ± 150[b]	14,985.6	14,521.4	15,397.6	–	Jessen et al., 2010
PS2863-1	162.5	15,660 ± 80	18,387.8	17,883.2	18,814.8	KIA-50401	This study
PS2863-1	168.5	17,700 ± 100	19,669.8	18,896.3	20,522.2	KIA-50402	This study
PS2863-1	199.5	19,140 ± 120	22,643.5	22,074.2	23,223.2	KIA-50403	This study
PS2837-5	10.5	535 ± 25	1,46.7	11.1	270.4	KIA 7570	Nørgaard-Pedersen et al., 2003
PS2837-5	50.5	2130 ± 40	1639.3	1451.7	1847.8	KIA 4652	Nørgaard-Pedersen et al., 2003
PS2837-5	76.5	3340 ± 35	3059.3	2858.5	3268.7	KIA 8927	Nørgaard-Pedersen et al., 2003
PS2837-5	111.5	4965 ± 45	5153.4	4908.1	5392.3	KIA 8928	Nørgaard-Pedersen et al., 2003
PS2837-5	153.5	7405 ± 45	7709	7483.3	7874.6	KIA 8929	Nørgaard-Pedersen et al., 2003
PS2837-5	182.5	8070 ± 60	8506.1	8322.7	8780	KIA 4653	Nørgaard-Pedersen et al., 2003
PS2837-5	225.5	9290 ± 60	10,0095.9	9823.6	10,499.3	KIA 8930	Nørgaard-Pedersen et al., 2003
PS2837-5	253.5	10,940 ± 50	12,243.5	11,886	12,354.8	KIA 7571	Nørgaard-Pedersen et al., 2003
PS2837-5	274.5	12,155 ± 60	13,411	13,151.6	13,620	KIA 10863	Nørgaard-Pedersen et al., 2003
PS2837-5	300.5	12,+655 ± 60	14,195.7	13,972.5	14,541.8	KIA 7572	Nørgaard-Pedersen et al., 2003
PS2837-5	359.5	12,940 ± 70	14,746	14,466.5	15,080.7	KIA 10864	Nørgaard-Pedersen et al., 2003
PS2837-5	382.5	16,040 ± 80	18,593.1	18,001.1	19,025.9	KIA 10865	Nørgaard-Pedersen et al., 2003
PS2837-5	389.5	17,440 ± 110	20,123.8	19,543.2	20,639.3	KIA 4654	Nørgaard-Pedersen et al., 2003
PS2837-5	415.5	24,230 ± 180	27,504.8	26,553.3	28,243.1	KIA 7573	Nørgaard-Pedersen et al., 2003

All ^{14}C dates are from *Neogloboquadrina pachyderma* (sinistral). The calibrated ages correspond to the modelled weighted mean age obtained after 8000 iterations executed with the Bacon 2.2 software (see text section 4).
[a] Ages obtained from correlation with core PS2837-5.
[b] Ages obtained from correlation with the western Svalbard magnetic susceptibility stack.

Dinocyst species were identified using the standardized taxonomy and nomenclature of Rochon et al. (1999). On average, 318 dinocysts were counted per sample except in the LGM samples (110 specimens on average) which are characterized by low concentrations. Dinocyst counts range from a minimum of 27 specimens at site PS2863 (LGM sample) to a maximum of 693 specimens counted in a late Holocene sample of site MSM5-712.

Reworked palynomorphs which result from the erosion of older sedimentary rocks and subsequent deposition (Streel and Bless, 1980) include pollen grains, spores, acritarchs as well as dinocysts. They were distinguished by a darker color and a flattened morphology owing to the longer preservation period in the sediment. A number of well-preserved palynomorphs identified at genus or family level to be stratigraphically older than Quaternary were also counted as reworked (cf. Williams and Brideaux, 1975). For example, specimens of the dinocyst *Wetzeliella* were identified and are stratigraphically associated with the Mid-Oligocene. When the source was terrigenous, reworked palynomorphs could be significantly older like *Neoraistrickia* and *Cicatricosisporites* which are pteridophyte spores from the Cretaceous.

Quantitative reconstructions of sea-surface parameters were made using the modern analog technique (MAT; Guiot, 1990), which was applied to the dinocyst assemblages. Although the MAT has been criticized as it possibly underestimates the error of prediction due to spatial autocorrelation (Telford, 2006; Telford and Birks, 2009), this approach remains more appropriate than calibration techniques for dinocyst-based reconstructions of sea-surface conditions and foraminifer-based reconstructions of sea-surface temperatures (e.g., Guiot and de Vernal, 2011). Here, we applied MAT following the procedure described by de Vernal et al. (2013). We have calculated the most probable values from a set of 5 analogs identified in the reference dinocyst database which includes data from the n = 1492 database (de Vernal et al., 2013) in addition to 284 new sites of which 28 are from the Greenland margins (cf. Allan et al., 2018) for a total of 1776 sites. The procedure consists of log-transformation of the occurrence (per mil) of 66 dinocyst taxa. The distance between modern and fossil spectra (sum of the differences in taxa occurrence expressed in log values) allows identifying the 5 best analogs. The most probable sea-surface values correspond to the average of the selected analogs,

weighted inversely to the distance. Poor analogs having a distance larger than a threshold value of 1.2 are excluded from the reconstructions. The uncertainty of sea-surface reconstructions or the error of prediction calculated from a subset (1/6) of the database are established at ± 1.3 °C and ±1.6 °C for the sea-surface temperatures in winter and summer, respectively, ± 2.1 psu for the salinity in summer and ±1.3 month/yr for the sea-ice cover (cf. Allan et al., 2018). The error of prediction is large for salinity due to the high variability in the low salinity domain. When considering only the >30 psu salinity range, the uncertainty is ±0.63 psu.

4. Chronology

The chronology of core MSM5-712 (Table 2; Fig. 2) is based on 18 accelerator mass spectrometry (AMS) ^{14}C dates obtained from planktic foraminifers (*Neogloboquadrina pachyderma*) and compiled by Müller et al. (2012) and Müller and Stein (2014). Additional age tie points were obtained from correlations with the total organic carbon content of PS2837-5 (81°13.99′N, 02°22.85′E; Nørgaard-Pedersen et al., 2003; see Fig. 1) and the western Svalbard reference stratigraphy of Jessen et al. (2010) (for details see Müller and Stein, 2014). A distinct interval of rapid sedimentation rate is well represented in core MSM5-712 between 657 and 433 cm.

The chronology of core PS2863-1 is based on five AMS ^{14}C dates on *N. pachyderma* (Table 2; Fig. 2). In addition, a sixth chronological tie point was obtained from stratigraphic correlation with the nearby core PS2837-5 (Fig. 1) from the western slope of the Yermak Plateau (Nørgaard-Pedersen et al., 2003). A well-defined IRD peak with similar thickness and coarse fraction content in the sediment sequence was found at 106.5 cm in core PS2863-1 and at 302.5 cm in core PS2837-5 (Fig. 2). In core PS2837-5, the peak has an age of 14,202 ± 285 cal. years BP, which was transferred to 106.5 cm in core PS2863-1. Further, a very fine grained laminated layer at 133-120 cm in core PS2863-1 was associated with a regional sedimentary event recorded all along the northwestern Barents Sea and the western Svalbard continental slopes up to the Yermak Plateau (Jessen et al., 2010; Lucchi et al., 2015). In Jessen et al. (2010), the interval started at 13,140 ± 150 ^{14}C years BP and ended at 12,840 ± 150 ^{14}C years BP, which corresponds to 14,931 ± 560 and 14,434 ± 620 cal. years BP, respectively. The rapidly deposited sediment in core MSM5-712 occurs within the limits of the unit described by Jessen et al. (2010) with a weighted mean age of 14,660–13,930 cal. years BP.

The age-depth relationship of cores PS2863-1, MSM5-712 and PS2837-5 was defined using the Bacon 2.2 software based on Bayesian statistics with default probability intervals of 95% (2-sigma) (Blaauw and Christen, 2011). All the original and correlated AMS ^{14}C ages were calibrated using the Marine13 calibration curve of Reimer et al. (2013) with an additional correction (delta R) of 98 ± 37 years calculated from six values from the Svalbard area (Olsson, 1980; Mangerud, 1972; Mangerud and Gulliksen, 1975) of the Marine Reservoir Data Base of Calib 7.1 (http://calib.org/marine/). All ages in this study are given as thousand calibrated years before present (ka), unless stated otherwise. We assumed that the surface of the cores was modern with a possible error of 460 years for core PS2863-1 and 160 years for core MSM5-712. Such errors were determined considering bioturbation in the upper ~3.5 centimeters. In other words, the errors are equivalent to the projected age at 3.5 cm. The average sedimentation rate of the rapidly deposited layer found in both cores is calculated to about 43 cm/kyr in core PS2863-1 and 309 cm/kyr in core MSM5-712. With exception of this layer, the mean sedimentation rate in core PS2863-1 is about 8 cm/kyr, which is much less than in core MSM5-712 characterized by mean sedimentation rates of 27 cm/kyr.

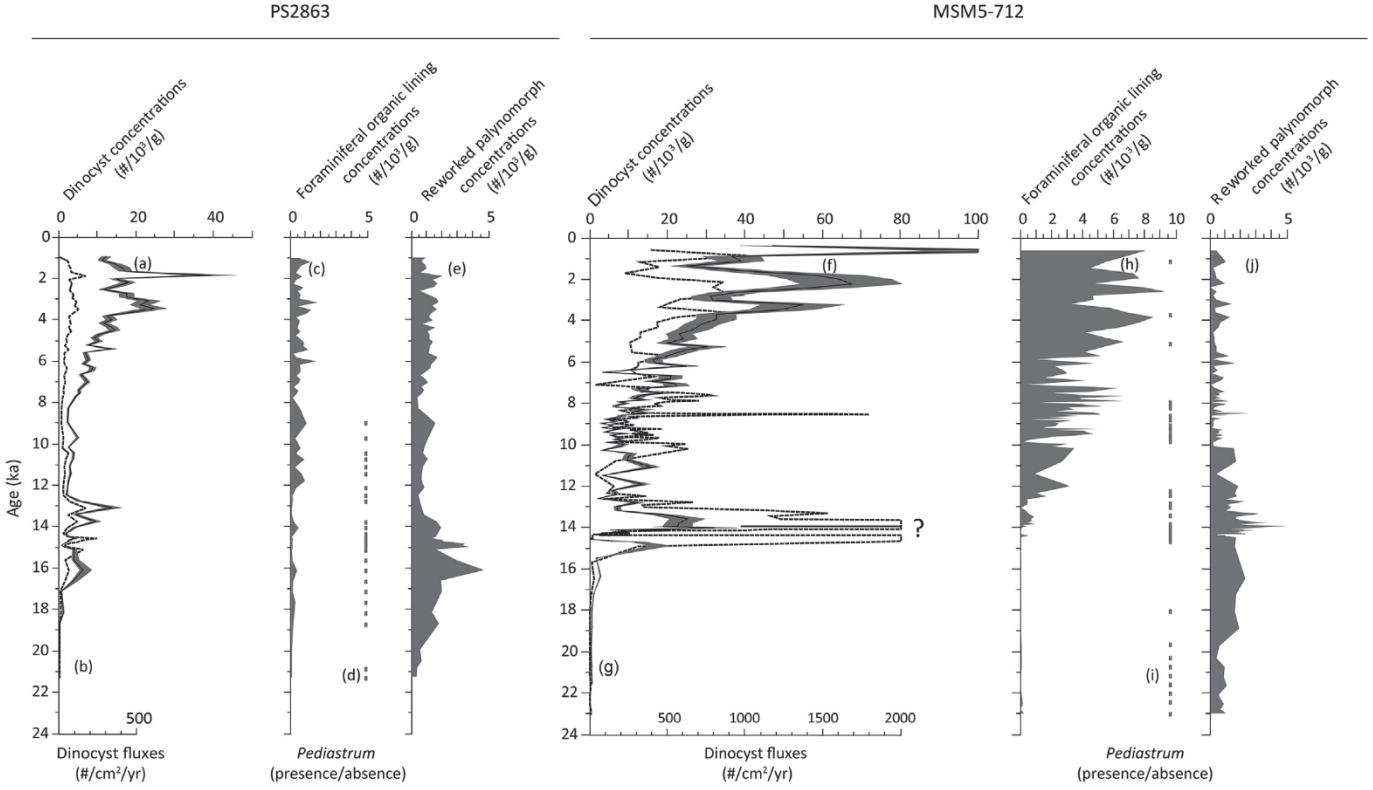

Fig. 3. Palynomorph concentrations at sites PS2863 and MSM5-712. The errors of dinocyst concentrations are illustrated by a gray shading. Dinocyst fluxes are represented by a dotted thick line.

5. Results

5.1. Palynological assemblages

Dinocysts largely dominate the palynological assemblages at both sites, MSM5-712 and PS2863, with concentrations recording similar positive trends towards present (Fig. 3a, f). Prior to 17 ka, dinocyst concentrations were low (150–800 cysts/g in MSM5-712 and 50–1000 cysts/g in PS2863). They were much higher after 17 ka (>2000 cysts/g in MSM5-712 and > 1000 cysts/g in PS2863) with exception of a marked minimum centered at 14.4 ka at site MSM5-712. The last 8000 years are characterized by very high concentrations ranging 10^4-10^5 cysts/g, with a maximum recorded in the upper part of the sequence representing the last 4000 years (Fig. 3a, f). Site MSM5-712 records about twice as high cyst concentrations as site PS2863. The concentrations led to calculated fluxes that are one order of magnitude higher in the late and postglacial sediments of core MSM5-712 (~800 cysts/cm^2/yr on the average) than those of site PS2863 (~60 cysts/cm^2/yr on the average) (Fig. 3b, g). Beyond these general characteristics, a double concentration peak is recorded at ~14.8 and ~13.9 ka in core MSM5-712 (Fig. 3f). Site PS2863 also recorded maximum concentrations centered at 13.7 and 13 ka (Fig. 3a). However, the peaks are less pronounced, possibly due to bioturbation and lower sedimentation rate at this site.

The concentrations of benthic foraminifer linings are ranging from 100 to 2000 linings/g in sediments of the last 14 ka at site PS2863 (Fig. 3c, h). In core MSM5-712, foraminifer lining concentrations continuously increased from 14 ka to present (2500 linings/g on the average), mirroring the trend in dinocyst concentrations, which both suggest a higher primary productivity after 14 ka and high organic carbon fluxes, especially during the Mid to Late Holocene (Fig. 3f, h). The concentrations of reworked palynomorphs range from 500 to 2000/g, with highest values in the 20–12 ka interval (Fig. 3e, j). The *Pediastrum* counts are low in all samples (<30 specimens; Falardeau, 2017) and their occurrence is thus reported as presence/absence (Fig. 3d, i). At site PS2863, *Pediastrum* is generally present throughout the record, from 23 to 8 ka, while at site MSM5-712 three intervals of occurrence are distinguished at 23–17 ka, at 14.5–12 ka and at 9.5–8 ka. At both sites, *Pediastrum* is nearly absent after 8 ka, with exception of three sparse occurrences at site MSM5-712 (Fig. 3d, i).

The dinocyst assemblages show high species diversity, with occurrences of both phototrophic and heterotrophic taxa at the two sites (Fig. 4). Among the phototrophic taxa, *Operculodinium centrocarpum*, *Nematosphaeropsis labyrinthus*, *Bitectatodinium tepikiense*, *Spiniferites elongatus* and *Spiniferites ramosus* dominate the assemblages, reaching more than 50% in some intervals. The accompanying taxa comprised the cyst of *Pentapharsodinium dalei*, *Impagidinium pallidum* and *Spiniferites* spp. (5–20%). Heterotrophic species are represented by *Brigantedinium* spp. and *Islandinium minutum* with low abundance of *Islandinium cezare* and *Selenopemphix quanta* (<5%). Dinocysts are present throughout the record, including heterotrophic taxa that are more sensitive to dissolution (cf. Kodrans-Nsiah et al., 2008), suggesting generally good preservation of organic-walled microfossils in the sediment. The dinocyst record is characterized by large variations in assemblages since the LGM. The major transitions are generally synchronous at both sites and the assemblages are similar, which allowed us to recognize five distinct dinocyst assemblage zones at

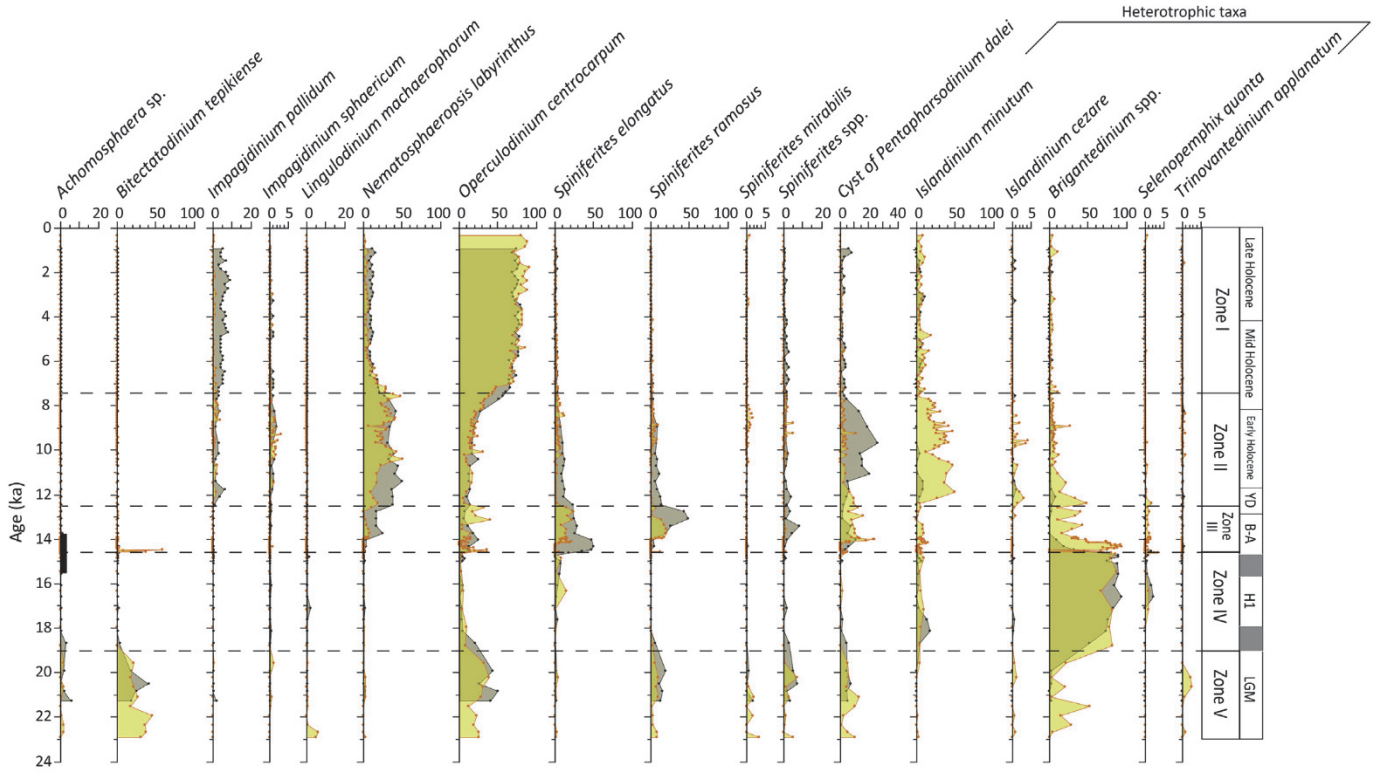

Fig. 4. Percentages of dinocyst taxa at site MSM5-712 (in light orange) superimposed on the percentages of dinocyst taxa at site PS2863 (in gray). Zones described in the text are delimited by horizontal dotted lines. The age of the LGM is established according to the MARGO working group (Kucera et al., 2005). The age of the Heinrich Stadial 1 (H1) is determined according to Gibb et al. (2014). Limits of the Bølling-Allerød (BA) and the Younger Dryas (YD) intervals are set according to Rasmussen et al. (2006); the divisions between Early, Mid- and Late Holocene follow suggestions by Walker et al. (2012). On the calibrated age axis, the black bar indicates the interval of the rapidly deposited sediment layer described by Jessen et al. (2010), including its 95% probability. (For interpretation of the references to color in this figure legend, the reader is referred to the Web version of this article.)

regional scale (Fig. 4).

In Zone V (~23–19 ka), the dinocyst assemblages are distinguished by abundant *B. tepikiense* reaching up to 40% in PS2863 and 46% in MSM5-712. The occurrence of this species is a characteristic feature of the LGM interval in the northern North Atlantic (de Vernal et al., 2005). According to its modern distribution, *B. tepikiense* tolerates high amplitude variations of seasonal temperature and relatively low salinity in stratified surface waters (Rochon et al., 1999; de Vernal et al., 2001, 2005). The occurrence of *O. centrocarpum*, which is a cosmopolitan species, is also high with a relative abundance of about 30%. Three peaks of *Brigantedinium* spp. (33%, 53% and 20%) are observed, but only at site MSM5-712. The dinocyst assemblages in core MSM5-712 also holds low but significant concentrations of more temperate species such as *Spiniferites mirabilis* (<3.5%) and *Lingulodinium machaerophorum* (<5%).

Zone IV, which spans ~19 to 14.7 ka, is characterized by the dominance of *Brigantedinium* spp. with relative abundance of 76–94% at site PS2863 and of 68–87% at site MSM5-712. The accompanying taxa include *I. minutum*, *S. elongatus* and *O. centrocarpum* (0–10%).

Zone III spans from 14.7 to 12.6 ka and covers most of the Bølling-Allerød interstadial (BA; 14.7–12.9 ka; Rasmussen et al., 2006). The boundary between zones III and IV corresponds to the base of the very high sedimentation rates layer. This sedimentary transition is also characterized in both dinocyst records by a subtle increase in *O. centrocarpum* and a more general increase of cysts from the genus *Gonyaulax,* represented notably by *S. elongatus* at site PS2863 and by *B. tepikiense* at site MSM5-712, together with a decrease of heterotrophic taxa (cf. *Brigantedinium* spp.). Zone III is characterized by short-lived variations of high amplitude in the dinocyst assemblages of both cores. It is also marked by some discrepancies between the two records. In particular, dinocyst assemblages of site PS2863 are mainly dominated by *Spiniferites* taxa, mostly *S. elongatus* from 14.7 to 13.7 ka and *S. ramosus* from 13.7 to 12.6 ka. In this interval, the specimens of *S. ramosus* include wide ranges of body size and shape, the length of processes and the presence/absence of an apical boss. They also include specimens with processes joined by more or less complete trabecula network, ranging from a typical *S. ramosus* to a *Nematosphaeropsis*-like morphology (see text section 6.2.3, Fig. 5). At site MSM5-712, the interval is characterized by a very short peak of *B. tepikiense* at 14.6–14.5 ka. *Brigantedinium* spp. dominates the assemblages from 14.5 to 14.1 ka. It is progressively replaced by *O. centrocarpum*, *S. elongatus*, *S. ramosus*, the cysts of *P. dalei* and *I. minutum*. At 13.2–12.6 ka, *O. centrocarpum* increases by about 10% at the expense of *S. ramosus*. Despite differences between the assemblages of Zone III, the two sites are characterized by significant occurrences of different morphotypes of *S. ramosus*.

Zone II covers the latest Pleistocene and the early Holocene (12.6–7.6 ka). It is characterized by high relative abundance of *O. centrocarpum* and the first significant occurrence of *I. pallidum*. Beyond these general features, there are differences in the dinocyst assemblages of the two cores. While the dinocyst assemblages in core MSM5-712 contain abundant heterotrophic taxa, especially *I. minutum* (10–50%) and *Brigantedinium* spp. (5–30%), the dinocyst assemblages at site PS2863 are almost entirely composed of phototrophic taxa such as *N. labyrinthus*, the cyst of *P. dalei* and *O. centrocarpum* (Fig. 4).

Finally, Zone I covers the interval from 7.6 ka to present. It is characterized by the dominance of *O. centrocarpum*, which constitutes about 70% of the assemblages at both sites. *N. labyrinthus* and *I. minutum* are the main accompanying taxa while *I. pallidum* records about 3–9% at site PS2863 but does not exceed 2% at site MSM5-712.

5.2. Reconstructions of sea-surface conditions

Application of MAT revealed close modern analogs, with 5 modern analogs used for the reconstruction in all samples. Distances between modern analogs and fossil assemblages are lower than 0.2 for most samples and never exceed the threshold value of 1.2 (Figs. 6f and 8f). Therefore, the reconstructions are as reliable as possible for most of the samples. Relatively large distances from modern analogs, however, are recorded between ~23 and 19 ka (mean of 0.62 and of 0.61 in MSM5-712 and PS2863, respectively), at ± 14.5 ka (mean of 0.46) and 10.7 ka (mean of 0.84) at site MSM5-712 and between 17.1 and 16.6 ka at site PS2863 (mean of 0.50) (Figs. 6f and 8f). In these intervals, one must be more cautious with quantitative estimates.

The reconstruction of sea-surface conditions from the MAT is generally coherent at the two sites (Fig. 9). From 23 to 7.6 ka, high amplitude changes of all parameters are recorded with a distinctive higher frequency between 14.7 and 13 ka, especially in core MSM5-712, whereas the establishment of more stable conditions similar to present ones occurred after 7.6 ka.

In Zone V spanning ~23–19 ka, sea-surface conditions reconstructed from the MAT point to a strong seasonality with high temperatures in summer (13–16.5 °C), but low temperatures in winter (1.7–1.9 °C) (Fig. 9a). Summer salinity is relatively low with a mean of 31.6 psu at site MSM5-712, but the mean is 1 psu higher at site PS2863 (Fig. 9b). Such conditions are compatible with estuarine and coastal environments, where modern analog assemblages are characterized by *B. tepikiense*. The occurrence of *Pediastrum* also indicates freshwater inputs (Figs. 6c and 8c). However, the reconstructions indicate almost no sea-ice cover and relatively high primary productivity (Fig. 6d–e, 8d-e), which can be challenged in the context of the LGM. Hence, intervals of low phytoplankton productivity (Rosell-Melé and Comes, 1999; Müller and Stein, 2014), as well as low dinocyst concentrations (de Vernal et al., 2005, 2006) were reported from the Nordic Seas during the LGM, which is coherent with the low dinocyst fluxes at the study sites (Fig. 3b, g).

Zone IV, from ~19 to 14.7 ka, corresponds to the coldest conditions of the entire record with extensive sea-ice cover (5–10 months/yr) and summer SSTs of about 4–5 °C at both sites (Fig. 9a, c). During this interval, sea-surface salinity remained low, of about 31.1 and 31.7 psu in summer, at sites PS2863 and MSM5-712, respectively (Fig. 9b).

In Zone III, spanning 14.7–12.6 ka, the two sites yielded different results in the first half of the zone (Fig. 9) as could be expected from the discrepancies in the dinocyst assemblages. The sea-surface estimates from site PS2863 indicate a reduced sea-ice cover extent (mean of 2.4 months/yr) and warmer summer conditions up to 12.3 °C, which corresponds to large seasonal contrasts of temperature (Fig. 8a, d). They also point towards saltier surface waters with an increase of about 1 psu (Fig. 8b). The estimates from core MSM5-712 suggest warm sea-surface conditions reaching about 12 °C in summer, similar as in PS2863, and relatively low SSSs (Fig. 6a and b), which is compatible with the occurrence of the *Pediastrum* related to freshwater inputs (Fig. 6c). The high temporal resolution of analyses in core MSM5-712 permitted to identify two short-lived events of large amplitude. One occurred at ~14.7–14.5 ka and corresponds to peaks of *B. tepikiense* and *O. centrocarpum*. The other occurred at ~14.5–14.1 ka concomitantly with a maximum abundance peak of *Brigantedinium* spp. (Fig. 7i, j, k). At 14.7 ka, a warm pulse is marked by summer SSTs up to 14.4 °C and 2 months/yr decrease in the sea-ice cover extent (Fig. 7a, e). In the first 100 years, the SSSs in summer were low with an average of 30.7 psu, but they increased up to 33.4 psu between 14.6 and 14.5 ka (Fig. 7c). In the 14.5–14.1 ka interval, colder conditions prevailed

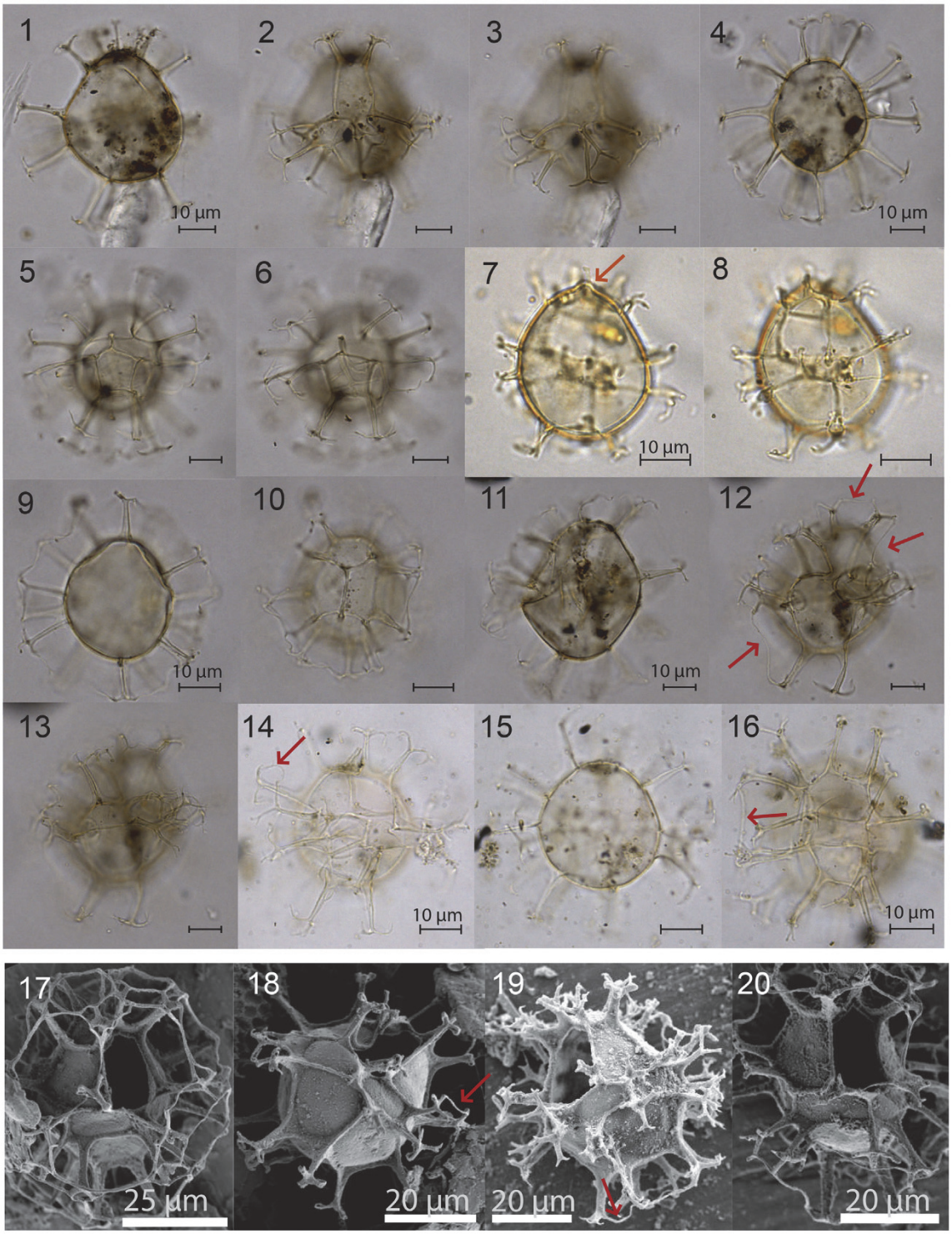

Fig. 5. Light micrographs and SEM photographs of the morphological variations of *Spiniferites ramosus* and *Nematosphaeropsis labyrinthus* in sediments of the 14.3–11.4 ka interval in cores PS2863-1 and MSM5-712.
1–3: Core PS2863-1, slide 3145-6E, 93–94 cm (EF G24/2). *Spiniferites ramosus* with an ovoid to a pear-shaped body. The gonal processes are shorter at the apex than at the antapex.
4–6: Core PS2863-1, slide 3145-6E, 93–94 cm (EF K20/2). *Spiniferites ramosus* with a spherical central body and long radial processes which have an equivalent length all around the cyst body. The specimen exposes long trifurcations and bifurcate tips.
7–8: Core PS2863-1, slide 3145-6C, 93–94 cm (EF L16/1). A small specimen of *Spiniferites ramosus* having aberrant morphologic characteristics like the development of an apical boss and a microgranular surface body. The processes are short and their tips are irregular.
9–10: Core PS2863–1, slide 3145-6E, 93–94 cm (EF G23/4). *Nematosphaeropsis labyrinthus* with a spherical body and solid processes. The cyst shows a particularly clear paratabulation.
11–13: Core PS2863–1, slide 3145-6E; 93–94 cm (EF G24/2). A large ovoid specimen of *Spiniferites ramosus* which developed a partial trabecular network.
14–15: Core MSM5–712, slide 2799–6; 410–411 cm (EF H22/1). Specimen of *Spiniferites ramosus* with a spherical body and relatively long trifurcations exposing at least one clear trabecula joining the distal ends of two adjacent processes.
16: Core MSM5–712, slide 2799–6; 410–411 cm (EF H17/3). Another specimen of *Spiniferites ramosus* exposing at least one clear trabecula.

with enhanced sea-ice cover reaching a maximum of 9 months/yr (Fig. 7e). The SSTs drastically decrease down to 0.8 °C, concomitantly with a drop in primary productivity and dinocyst concentrations (Fig. 7a, g, h). The SSSs remained relatively low with an average of 31.6 psu.

In Zone II, spanning 12.6 to 7.6 ka, summer SSTs decrease to a mean of 5.5–6 °C at both sites, which resulted in a reduced amplitude of seasonal temperatures (Fig. 9a). The SSSs increased from 32.2 to 34.3 psu at site PS2863 and from 30.5 to 33.5 psu at site MSM5-712 (Figs. 6b and 8b). The sea-ice cover increased to a maximum of 5 months/yr at 11.4 ka at site PS2863 and to an average of 7 months/yr at 11.9–10.7 ka at site MSM5-712, prior to a decrease to 1–2 months/yr towards the end of the interval (Figs. 6d and 8d).

In Zone I, corresponding to the last 7600 years, summer SSTs remained relatively stable with values of about 4.5 °C and 4.0 °C at sites PS2863 and MSM5-712, respectively (Fig. 9a). However, a decrease of about 1.5–2 °C in winter SSTs and an increase of 1–2 months/yr in sea-ice cover are recorded towards modern (Fig. 9a, c). Estimated summer SSSs decrease by about 1 psu at site PS2863. A less pronounced decrease of SSSs is recorded in core MSM5-712.

6. Discussion

6.1. The LGM paradox

During the LGM, hydrographical conditions in the Nordic Seas were probably unique with no perfect modern equivalent (cf. de Vernal et al., 2005, 2006, Figs. 6f and 8f). The selected modern analogs of the LGM in our study cores were obtained from the northeastern shore of the United Sates, the northern margin of Norway and the Gulf of St. Lawrence where large amplitude seasonal gradients of temperature presently prevail due to estuarine-type circulation. Such conditions do not exist in open ocean settings such as Fram Strait today. Hence, the quantitative reconstructions of the LGM must be interpreted with caution. In a context of low dinocyst concentrations, there is also a risk of distortion of the signal due to distal input. However, this is unlikely here considering the similarity of assemblages at both sites, MSM5-712 and PS2863, which are located 200 km apart from each other.

Despite the low concentrations, the dominance of phototrophic taxa (Fig. 4) provides evidence for open water conditions in eastern Fram Strait during the LGM, at least episodically. This was previously inferred, not only from dinocysts (de Vernal et al., 2000, 2005), but also from coccoliths (Hebbeln and Wefer, 1997; de Vernal et al., 2000), alkenones (Rosell-Melé and Comes, 1999), IP_{25} biomarkers (Müller and Stein, 2014; Xiao et al., 2015) and planktic foraminifers (Hebbeln et al., 1994; Sarnthein et al., 1995, 2003; Weinelt et al., 1996, 2003; Nørgaard-Pedersen et al., 2003; Pflaumann et al., 2003; Zamelczyk et al., 2014). Seasonally open water conditions may even have prevailed along the northern continental slope of Svalbard, where high fluxes of planktic and benthic foraminifers were recorded (Chauhan et al., 2014, 2016). Open waters, at least seasonally, in the Nordic Seas were probably an essential moisture source for the rapid growth of the Svalbard Barents Sea ice sheet (SBSIS) (Hebbeln et al., 1994). There is also ample evidence for strong subsurface inflow of AW to the Nordic Seas, the Fram Strait and northern Svalbard during the LGM based on planktic foraminifer concentrations and assemblages (Rørvik et al., 2013; Chauhan et al., 2014, 2016), good calcium carbonate preservation (Zamelczyk et al., 2014) and the $\delta^{18}O$ signals of planktic foraminifers (Nørgaard-Pedersen et al., 2003; Rasmussen and Thomsen, 2008). Mg/Ca data in ostracods from the Arctic Ocean (Cronin et al., 2012) also point to a strong inflow of AW, even warmer than at present, but probably at a greater depth. The paleoceanographical records of the LGM are therefore paradoxical as they may suggest relatively warm conditions in Fram Strait despite generally cold climate.

The inflow of AW in the context of a heavily glaciated environment might have led to high meltwater inputs and low surface salinity as indicated by the relative abundance of *B. tepikiense* (Fig. 4). Stratified low density surface waters could have resulted in low thermal inertia (low heat capacity). This would be coherent with the very large amplitude of seasonal temperatures which were marked by freezing conditions in winter and relatively warm summers (Fig. 9a). Despite uncertainties due to possible reworking, alkenone data also suggest relatively warm sea-surface conditions in the area (Rosell-Melé and Comes, 1999). A scenario of stratified surface water masses during the LGM, which would have confined the AW at the subsurface, was proposed by Bauch et al. (2001). However, in our dinocyst assemblages, the presence of *O. centrocarpum* reflects phototrophic productivity in surface water and would relate to AW (Rochon et al., 1999; Grøsfjeld et al., 2009), leading to hypothesize advection of AW during the LGM. The paradoxically high summer SSTs during the LGM might therefore be linked to low thermal inertia of the upper waters. Alternatively, it may be related to occasional advection of AW at the surface.

A flow of AW near the surface, even occasional, and the relatively low salinity that apparently prevailed throughout the LGM in the uppermost water layer are equivocal. Since the percentages of *O. centrocarpum* are half of those recorded during the Mid-Late Holocene (Fig. 4), surface conditions related to AW advection probably differed from the modern situation and were possibly weakened or highly variable due to freshwater discharges. de Vernal et al. (2006) proposed that sea-surface conditions in the Nordic Seas were unstable during the LGM, with alternation of relatively warm episodes due to strong northward AW fluxes and cold episodes with high meltwater discharge and dense sea-ice cover. For instance, the dinocyst record of core MD95-2010 in the southern Norwegian Sea pointed to very large amplitude centennial variations of sea-surface conditions during the LGM, with oscillations between 0 and 6 months/yr of sea-ice cover and evidence of episodic high SSTs (cf. Eynaud et al., 2004; de Vernal et al., 2006). The high-resolution record of Müller and Stein (2014) also pointed to rapidly changing conditions from perennial to reduced sea-ice cover (Fig. 10b) in response to perturbations in the advection of AW. Similarly, inflow of relatively warm AW but unstable conditions in subsurface waters were reported from foraminifer data (Rasmussen and Thomsen, 2008; Rørvik et al., 2013). Large instabilities with rapid perturbations of AW advection might correspond to the prompt response of the AMOC to iceberg discharges and pulses of meltwaters during the LGM (Levine and Bigg, 2008). Unfortunately, the current temporal resolution of our records in addition to uncertainties due to limited biogenic material in LGM sediment from Fram Strait does not permit to clearly identify short-lived fluctuations in SSSs.

A possibility to explain the dinocyst assemblages of the LGM

17: Core PS2863-1, sample 3145–5, 89–90 cm. SEM photograph of a *Nematosphaeropsis labyrinthus* specimen with a particularly well-developed paratabulation with large sutural ridges and solid processes.

18–19: Core PS2863-1, sample 3145–5, 89–90 cm. SEM photographs of two different specimens of *Spiniferites ramosus* exposing random processes being connected by a single trabecular liaison, at the cingulum (18) and at the antapex (19).

20: Core PS2863-1, sample 3145–5, 89–90 cm. SEM photograph of a *Spiniferites ramosus* specimen with an almost complete trabecular network.

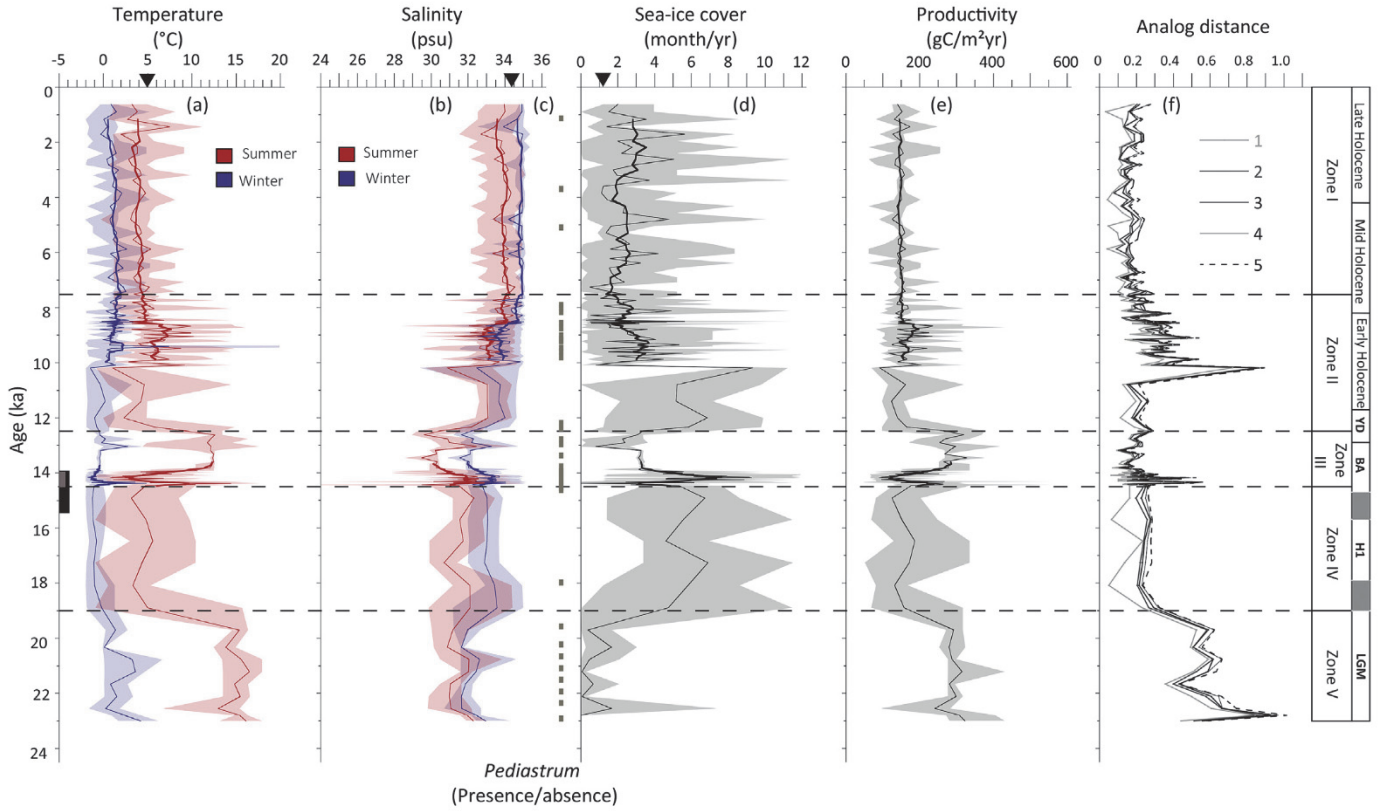

Fig. 6. Reconstructions of sea-surface conditions at site MSM5-712 including (a) summer and winter SSTs in red and blue, respectively, (b) summer and winter SSSs in red and blue, respectively, (c) gray dots indicating samples with at least one colony of *Pediastrum*, (d) sea-ice cover duration, and (e) productivity. Mean values are represented by a thin line, the thick line shows a five-point running average. Maximum and minimum values are represented in brighter shading. In (f) is the distance of the five closest analogs. Black triangles indicate modern values at the core site (SSTs and SSSs in summer) from the World Ocean Atlas 2001 (Conkright et al., 2002) and the average sea-ice cover extent from NSIDC data. Zones as described in the text are divided by horizontal black dotted lines. On the calibrated age axis, the black bar indicates the interval of the rapidly deposited sediment layer as defined by Jessen et al. (2010), including its 95% probability while the gray bar represents the rapidly deposited sediment layer at the site. (For interpretation of the references to color in this figure legend, the reader is referred to the Web version of this article.)

could be a deposition to the sea floor only during brief intervals of relatively warm conditions, thus representing extremes instead of average conditions and resulting in a warm bias in quantitative estimates. Such a hypothesis was previously put forward by Nørgaard-Pedersen et al. (2003) and Weinelt et al. (2003). If correct, the low dinocyst concentrations could relate to dinoflagellate populations and cyst fluxes to the sea floor during phases of sea ice-free conditions while intervals characterized by permanent sea-ice cover correspond to almost nonexistent phytoplankton productivity as suggested from biomarker studies in core MSM5-712 by Müller and Stein (2014). The low dinocyst concentrations in the LGM sediment would therefore be the result of dilution of biogenic fluxes during brief episodes of productivity with barren sediments accumulated under quasi-perennial sea-ice cover. Considering mean annual fluxes of dinocysts (~50 cysts/cm^2) at site PS2863 since 18.5 ka, we calculate that the average dinocyst content in LGM sediment (~1 cyst/cm^2/yr; Fig. 3b) represents productivity 50 times lower or an equivalent productivity occurring only during exceptional summers, most of the interval being otherwise characterized by perennial sea ice and zero dinocyst flux. In the latter case, which is likely in our view, we may calculate that sea ice-free conditions in northeastern Fram Strait occurred only a couple of years per century during the LGM, possibly as polynyas opened by katabatic winds from the SBSIS. However, higher temporal resolution is needed for a clear demonstration and unequivocal assessment of inter-annual variability of sea-surface conditions in eastern Fram Strait.

6.2. Transition from the LGM to the postglacial

6.2.1. The early deglaciation and Heinrich Stadial 1

The transition from Zone V to Zone IV at about 19 ka is characterized by an important change in assemblages with the decrease of *O. centrocarpum* and the augmentation of the heterotrophic taxa *Brigantedinium* spp. and *I. minutum*. It corresponds to a change towards particularly cold conditions and dense sea-ice cover (Fig. 9a, c; cf. Rochon et al., 1999; de Vernal et al., 2001, 2013), which is coherent with a decrease in the percentages of subpolar species in planktic foraminifer assemblages of the eastern Fram Strait during the same interval (Zamelczyk et al., 2014). This transition occurred concomitantly with an increase of reworked palynomorphs at both core sites (Fig. 3e, j) pointing to intense glacial erosion, which closely followed the IRD signal recorded at 20.5 ± 0.5 ka on the western Svalbard slope (Jessen et al., 2010). The cooling after ~19 ka probably occurred in an early phase of the SBSIS deglaciation recorded at about 19–17 ka in the Fram Strait (Hebbeln et al., 1994; Andersen et al., 1996; Landvik et al., 1998; Nørgaard-Pedersen et al., 2003; Rasmussen et al., 2007). Decreased summer SST and enhanced sea-ice cover extent after 19 ka were suggested to result from reduced AW inflows towards the end of the LGM (Rasmussen et al., 2007). This is coherent with the lowest relative abundance of *O. centrocarpum* (Fig. 4).

The low SSSs in both core records that characterize Zone IV (<33 psu; Fig. 9b) and the high concentrations of *Pediastrum* only at site PS2863 (Falardeau, 2017), indicating a northern source of

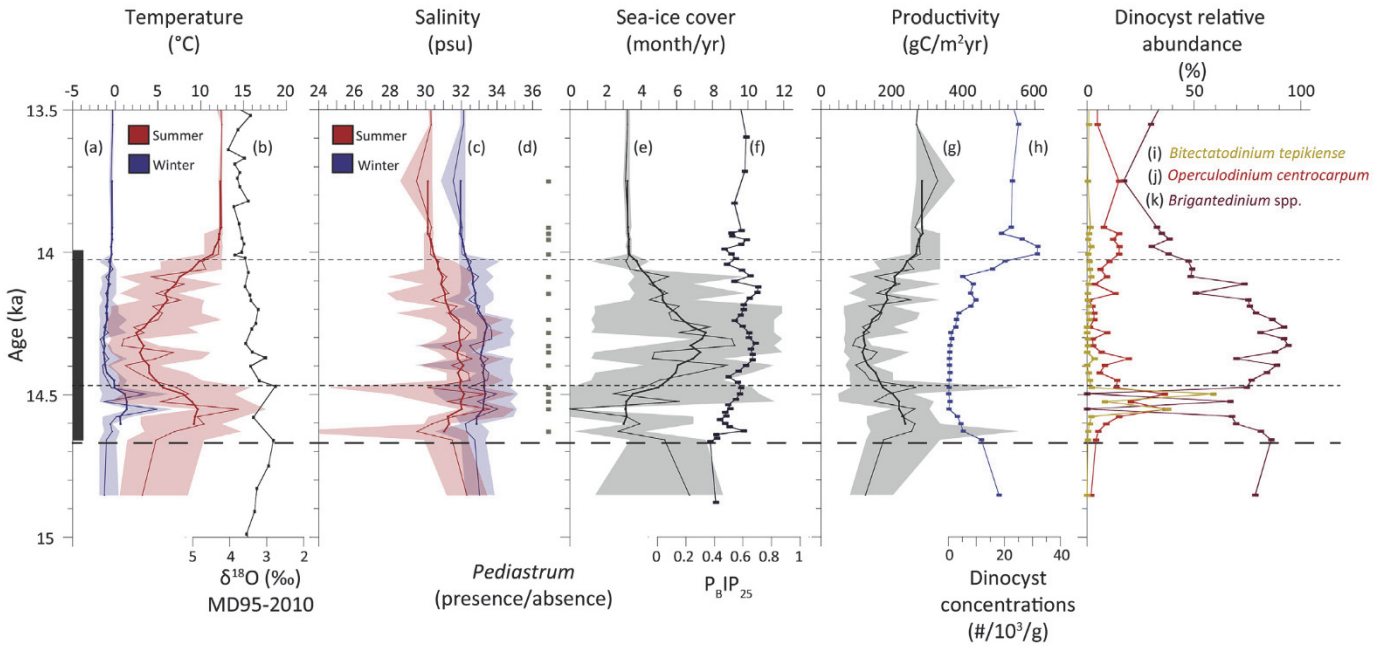

Fig. 7. Close-up of sea-surface conditions at site MSM5-712 during the BA interstadial including (a) summer and winter SSTs in red and blue, respectively, (b) $\delta^{18}O$ of planktic foraminifer *N. pachyderma* (sinistral) tests in core MD95-2010 in black (Dokken and Jansen, 1999), (c) summer and winter SSSs in red and blue, respectively, (d) occurrence of at least one colony of *Pediastrum* marked by gray dots, (e) sea-ice cover durantion, (f) sea-ice cover proxy P_BIP_{25} in dark blue (Müller et al., 2012; Müller and Stein, 2014), (g) productivity, (h) dinocyst concentrations in light blue in addition to (i-j-k) percentages of three dinocyst taxa relevant in this time interval. The two finer dotted lines indicate the limits of a cooling event (see text section 6.2.2). The vertical gray bar represents the rapidly deposited sediment layer at the site. (For interpretation of the references to color in this figure legend, the reader is referred to the Web version of this article.)

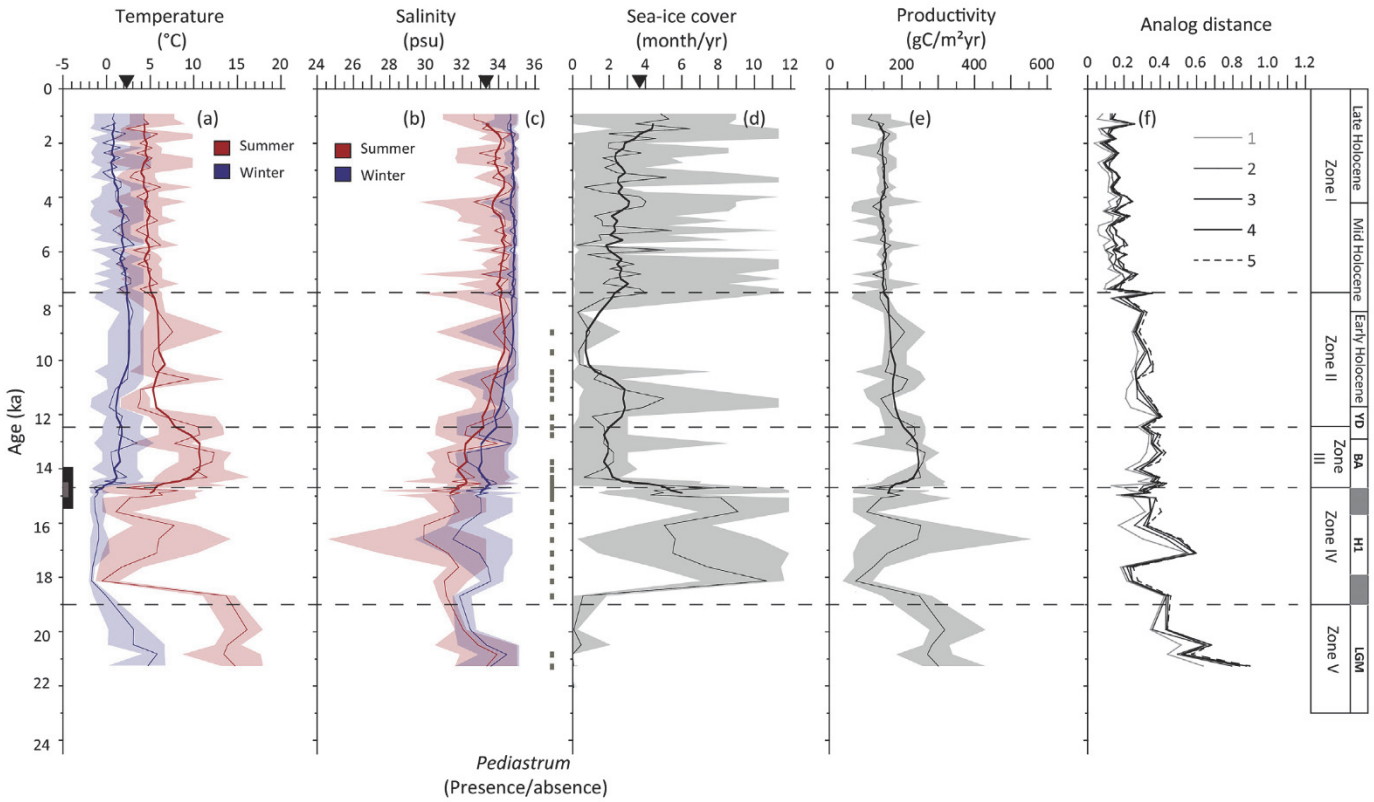

Fig. 8. Reconstructions of sea-surface conditions at site PS2863 including (a) summer and winter SSTs in red and blue, respectively, (b) summer and winter SSSs in red and blue, respectively, (c) gray dots indicating samples with at least one colony of *Pediastrum*, (d) sea-ice cover duration, (e) productivity, and (f) the distance of the five closest analogs. For explanations see Fig. 6. (For interpretation of the references to color in this figure legend, the reader is referred to the Web version of this article.)

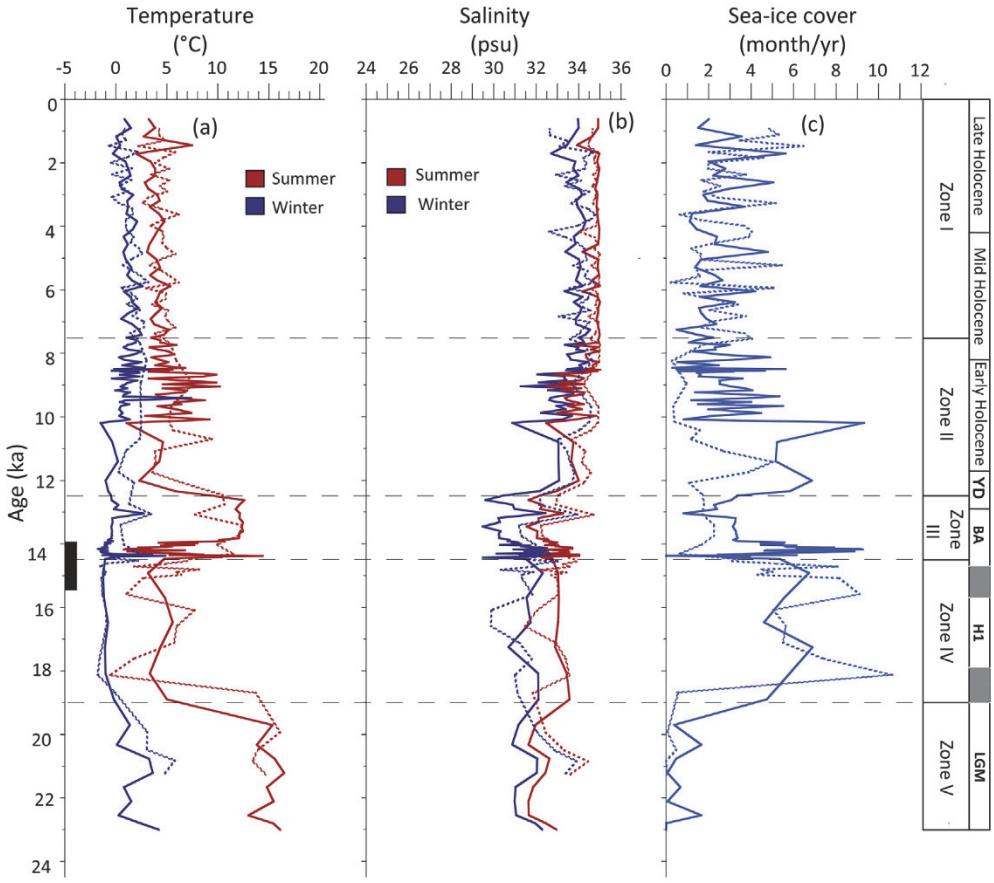

Fig. 9. Reconstructions of sea-surface conditions at site PS2863 (dotted lines) superimposed by the reconstructions of sea-surface conditions at site MSM5-712 (uniform lines) including (a) summer and winter SSTs in red and blue, respectively, (b) summer and winter SSSs in red and blue, respectively, (c) sea-ice cover duration. Only mean values are presented. On the calibrated age axis, the black bar indicates the interval of the rapidly deposited sediment layer as defined by Jessen et al. (2010), including its 95% probability. (For interpretation of the references to color in this figure legend, the reader is referred to the Web version of this article.)

freshwaters, suggest large meltwater and iceberg discharges from the SBSIS. Meltwater flow probably led to cold and buoyant surface waters, which would be at the origin of the near shutdown of the AMOC at about 18–17.5 ka (McManus et al., 2004; Hall et al., 2006; Stanford et al., 2011; see Fig. 10h) and low $\delta^{18}O$ of planktic foraminifers in the Nordic Seas during the same interval (Jones and Keigwin, 1988; Lehman et al., 1991; Hebbeln et al., 1994; Bauch et al., 2001; Nørgaard-Pedersen et al., 2003; Rasmussen et al., 2007). Such a scenario supports the hypothesis of Ivanovic et al. (2017) based on coupled model experiments, which suggests that the acceleration of the Eurasian deglaciation at ~18.5 ka and freshwater/meltwater delivered to the Arctic Ocean are at the origin of the Heinrich Stadial 1 (H1). Hence, Zone IV would correspond to an interval that can largely be associated with the H1 (Stern and Lisiecki, 2014). The reduced AMOC strength and cooling in the northern North Atlantic would have preceded the Laurentide Ice surge in Hudson Strait (e.g., Heinrich, 1988; Bond et al., 1993; Hemming, 2004), which has been dated from 17.9 to 15.7 ka in a detailed Labrador Sea record (Gibb et al., 2014).

Consistent with our dinocyst assemblages, the P_BIP_{25} data suggest dense sea-ice coverage, but mostly from 19 to 17.5 ka (Müller and Stein, 2014, Fig. 10b). An increase in primary productivity can be deduced from biomarker data after 17.5 ka (Müller and Stein, 2014), which is synchronous with the increase in dinocyst concentrations in both core records presented here (Fig. 3a, f). Generally, the shift at 17.5–17 ka suggests a transition from an extremely harsh environment during the earliest phase of the deglaciation to more favorable and milder pelagic conditions, which is in line with planktic foraminifer data from the Yermak Plateau (Chauhan et al., 2014). The abrupt shift from a heavily glaciated environment to seasonal sea-ice at that time, as deduced from the P_BIP_{25} index (Müller and Stein, 2014), could illustrate this change in primary producer conditions.

6.2.2. *The rapidly-deposited detrital layer and Bølling-Allerød*

At the base of Zone III, which is also marked by the rapidly deposited sediment layer, there is a peak of high summer SSTs accompanied by reduced sea-ice cover (Fig. 7a, e). This warm event is observed in core MSM5-712, probably because of the high temporal resolution of analyses that permits to identify short-lived events. The transition from Zone IV to III, characterized by increase in *O. centrocarpum,* probably corresponds to enhanced AW contribution (Fig. 7j). It occurred near-synchronously with the resumption of the AMOC at about 14.6 ka, coincident with the BA warming (McManus et al., 2004; Stanford et al., 2011; see Fig. 10h). Enhanced AW contribution probably led to regional warming, glacier retreat, meltwater inputs and low salinity as suggested by the excursions of *B. tepikiense* (Fig. 7i), the recurrence of the *Pediastrum* (Fig. 6c) and minima in $\delta^{18}O$ recorded in *N. pachyderma* shells from core MD95-2010 (Dokken and Jansen, 1999; see Fig. 7b). At that time, benthic foraminifer assemblages indicate a shift from polar to subarctic conditions along the western Svalbard margin (Ślubowska-Woldengen et al., 2007, 2008).

At 14.5 to 14.1 ka, shortly after the warm interval, our sea-

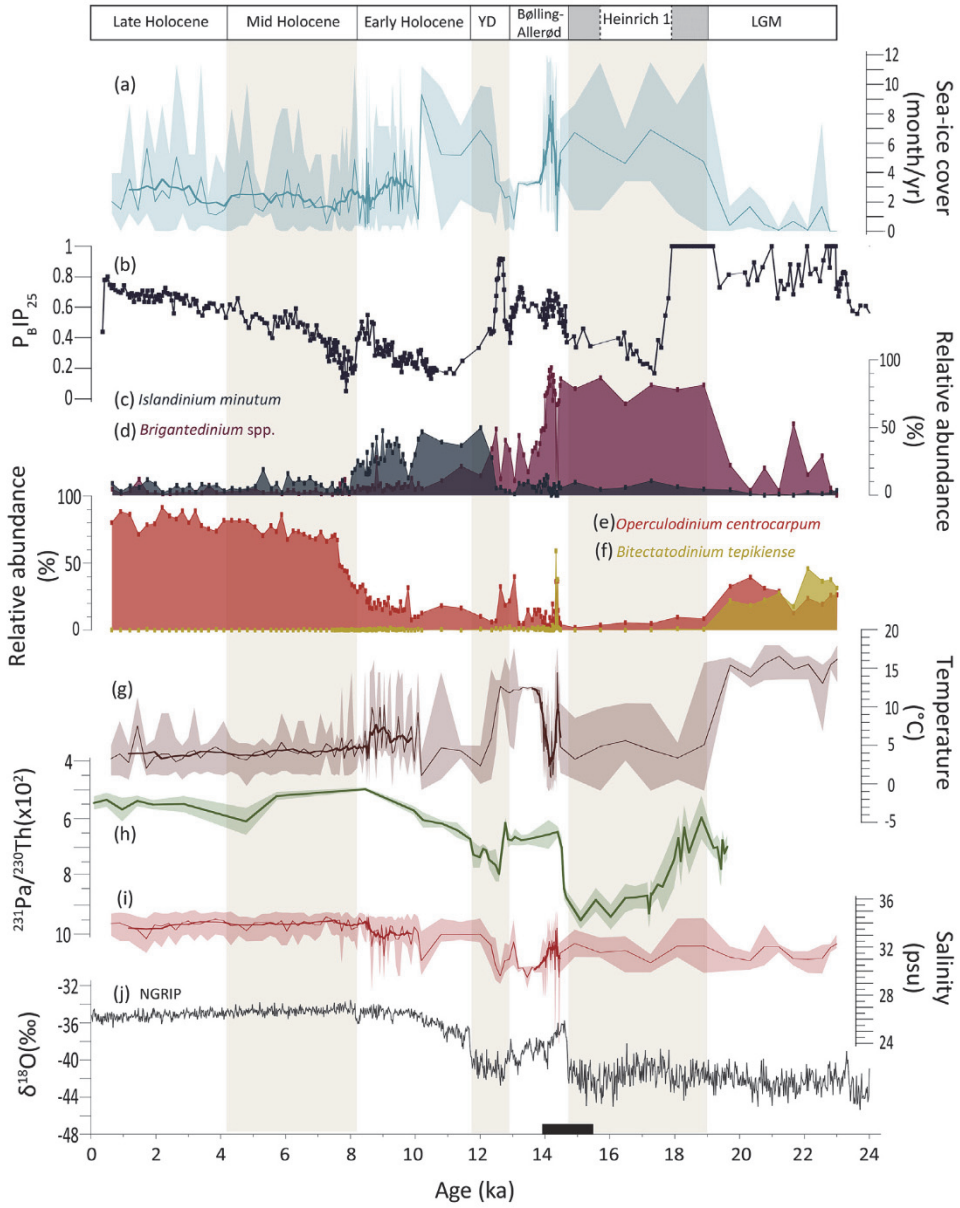

Fig. 10. Sea-surface reconstructions at site MSM5-712 including (a) sea-ice cover seasonal duration to be compared with (b) the P_BIP_{25} index from Müller et al. (2012) and Müller and Stein (2014) represented by a dark blue line. Data are presented with the chronology described in this paper to permit better correlations with our records. Percentages of heterotrophic taxa (c) *I. minutum* are in blue and (d) *Brigantedinium* spp. in purple and percentages of phototrophic taxa (e) *O. centrocarpum* are in orange and (f) *B. tepikiense* in yellow. The figure also illustrates (g) SSTs in summer (red) and winter (blue), (h) the $^{231}Pa/^{230}Th$ record (green) as a proxy of AMOC strength (McManus et al., 2004), (i) SSSs in summer (red) and winter (blue) and (j) $\delta^{18}O$ data (gray) from the NGRIP ice core (Andersen et al., 2004b). On the calibrated age axis, the black bar indicates the interval of the rapidly deposited sediment layer defined by Jessen et al. (2010), including its 95% probability. (For interpretation of the references to color in this figure legend, the reader is referred to the Web version of this article.)

surface reconstructions indicate a completely reversed trend, with the recurrence of *Brigantedinium* spp. (Fig. 7k) and the onset of extremely cold conditions with extensive sea-ice cover (Fig. 7a, e). This cold event covers the larger part of the rapidly deposited layer, which was dated of 14,700 to 13,900 cal. years BP in core MSM5-712. This layer is probably the same as the one on the upper continental slope of the Storfjorden identified by Lucchi et al. (2015). It bears sedimentological features similar as those of the deposit described by Jessen et al. (2010) from the western Svalbard and the Yermak Plateau continental slopes. Hence, this sedimentological event might be of high significance in the deglacial history of the SBSIS as it would originate from the scouring of the northwestern Barents Sea continental shelf in response to a major ice sheet collapse (Lucchi et al., 2015). The timing of such a collapse is coherent with the SBSIS limit of Hughes et al. (2016), showing that the ice sheet extending to the central Barents Sea and Bjørnjøya retreated between 15 and 14 ka. The rapid ice collapse might have been triggered by the enhanced AW advection and related warming of surface water as documented above, together with a eustatic sea level rise. The palynological content of the rapidly deposited layer at both sites is characterized by a maximum in reworked palynomorphs (Fig. 3e, j), implying erosional processes on the shelves and subsequent outwash deposition. Our data thus suggest that this layer was formed from the erosion and deposition of sediments originating from the northwestern Barents Sea continental shelf. Furthermore, the occurrence of thermophilic and diversified

dinocyst assemblages at the very base of the rapidly deposited layer supports the hypothesis of a warm pulse at the onset of the sedimentological event that has marked the continental margins on a regional scale.

The low dinocyst concentrations (mean of 390 cysts/g) in sediments accumulated from 14.5 to 14.3 ka (Fig. 7h) likely result from dilution with sediments from a sediment-laden meltwater plume. Nevertheless, the calculated fluxes are about 140 cysts/cm^2/yr during this interval, which corresponds to relatively high fluxes and productivity.

From 14.1 to 12.6 ka (top of Zone III), recurring high SSTs possibly relate to enhanced AW heat advection (Fig. 6a). However, while subpolar conditions are recorded in bottom waters around Svalbard (Bartels et al., 2017), particularly between 14.5 and 13.5 ka (Ślubowska-Woldengen et al., 2007), the planktic foraminifer assemblages rather indicate polar conditions during the BA interstadial (Rasmussen et al., 2007; Aagaard-Sørensen et al., 2014b; Chauhan et al., 2014), probably linked to heat loss to the atmosphere and/or outpouring of cold waters as suggested by Rasmussen et al. (2007).

At the study sites, the SSTs are marked by high seasonal amplitudes from winter to summer (Fig. 9a). Strong inflow of AW during the deglaciation probably initiated atmospheric warming at the margin of the SBSIS and enhanced meltwater discharge, leading to low salinities and a strong stratification of surface water. The low δ^{13}C of *N. pachyderma* in core MSM5-712 throughout the BA also suggests stratification in the water column (Aagaard-Sørensen et al., 2014b). Hence, the high SSTs in summer can be ascribed to a low thermal inertia of the surface water layer together with heat advection from AW. Enhanced ice calving and meltwater discharge during the Allerød are indicated by coarse sediment and low δ^{18}O from foraminifer shells (Andersen et al., 1996; Hald et al., 2001; Jessen et al., 2010; Zamelczyk et al., 2012; Aagaard-Sørensen et al., 2014b; Bartels et al., 2017). The extensive sea-ice cover reconstructed from the P_BIP_{25} index during most of the BA was associated with stratification related to meltwater discharge (Müller and Stein, 2014), which is compatible with our interpretation.

The hypothesis of AW advection that would lead to enhanced meltwater inputs during deglacial phases could explain the reverse relationship between the SSS and the δ^{18}O at NGRIP during the Allerød period (Fig. 10i and j). In opposite situations, low summer SSTs could suggest weakened inflow of AW, less stratified surface waters with high thermal inertia or a vertical mixing of water masses. Therefore, in contrast to intervals of high summer SSTs and large seasonal contrasts, the low summer SST phases were not associated with pronounced SSS decreases during the deglaciation.

6.2.3. The Spiniferites ramosus morphotypes and sea-surface conditions at 14.1–12.9 ka

The dinocyst assemblages of the Allerød interval (14.1–12.9 ka; Rasmussen et al., 2006) are characterized by abundant specimens of *Spiniferites*, including the cosmopolitan species *S. ramosus* (Fig. 4), and by the presence of a large variety of morphotypes, ranging from typical *S. ramosus* to *Nematosphaeropsis*-like morphologies (Fig. 5). This is particularly the case at ~13.4 ka where the highest concentrations of *Spiniferites* are recorded, but other atypical specimens were observed from 14.3 to 11.4 ka. The two dinocyst species *S. ramosus* and *N. labyrinthus* are related to the same motile dinoflagellate species *Gonyaulax spinifera* (Dodge, 1989). From culture experiments, Rochon et al. (2009) proposed that they could be the two endmembers of the same genotype or at least related species. According to Rochon et al. (2009), the different phenotypes only occur in salinities between 25 and 30 psu, whereas typical *S. ramosus* and *N. labyrinthus* are usually more abundant in saltier water of 32–36 psu and 31–37 psu, respectively (Rochon et al., 1999; Marret and Zonneveld, 2003). Ellegaard (2000) also found unusual cyst morphotypes more abundant during low salinity events in the last 2000 years in the Limfjorden, northern Denmark. Other morphological disparities seem to be a response to salinity constraints, like the processes length of *O. centrocarpum* (Mertens et al., 2012) or the development of cross-shaped cysts in the Black Sea during the Late Pleistocene (Rochon et al., 2002). From 14 to 12.6 ka, the analogs selected for the MAT reconstructions are mainly from the Gulf of St. Lawrence. However, analogs were also obtained from the Barents Sea off northern Norway and the northeast shore of the United States. While all these analogs are associated with warm summers (>8 °C), they relate to variable salinities ranging from <31 psu in the Gulf of St. Lawrence to oceanic conditions at some other analog locations. In our cores, the morphotypes occurred mostly in intervals of low reconstructed SSSs, with exception of a few high-salinity excursions, notably at 13 ka (33.9 psu) at site PS2863 (Fig. 8b) and at 13.2 ka (32.4 psu) at site MSM5-712 (Fig. 6b). Hence, the interval from 14 to 12.6 ka was apparently characterized by unstable conditions with high amplitude variations of SSSs and large seasonal contrasts of temperatures, as it is often the case in nearshore environments. The episode of strongly reduced SSSs we calculate from core MSM5-712 at 14–12.6 ka coincides with accelerated glacial retreat around Svalbard (e.g., Andersen et al., 1996; Hald et al., 2001). Hence, morphological variations of processes during cyst formation may result from reduced salinities as proposed by Rochon et al. (2009). Highly variable conditions and/or a turbulent environment can also have impacted the cyst morphology.

6.2.4. The Younger Dryas interval

At the studied sites, the Younger Dryas interval (YD; 12.9–11.7 ka) as defined by Rasmussen et al. (2006) corresponds to a transition from large regional meltwater discharges resulting in low salinities of <32 psu (Zone III) to modern-like thermohaline properties in surface waters (Zone II; Fig. 9b). The occurrence of *I. pallidum* at 12.5 ka marked this transition in the dinocyst assemblages at both sites, especially at site PS2863 where it is more pronounced (Fig. 4). The first postglacial occurrence of *I. pallidum* was reported by Matthiessen and Baumann (1997) at ~12.9 ka from core PS1295 (see Fig. 1). This taxon is a typical component of the modern assemblages in the Nordic Seas and indicates cold ocean conditions (Matthiessen, 1995; Rochon et al., 1999; Grøsfjeld et al., 2009; Bonnet et al., 2010). A change in the benthic fauna around Svalbard is also reported to have occurred at 12.5 ka as the result of recurring cold bottom waters (Ślubowska-Woldengen et al., 2007, 2008). The planktic foraminifer assemblages that continued to be dominated by *N. pachyderma* during the BA also indicate cold conditions (Rasmussen et al., 2007; Aagaard-Sørensen et al., 2014b). In surface waters, our data indicate a strong cooling with a decrease of SSTs by about 10 °C in summer (Fig. 9a). The cooling was accompanied by an increase in SSSs, from 31 to 33 psu (Fig. 9b), which is probably related to reduced meltwater discharges during a slowdown of the ice sheet retreat, as indicated by a stabilization of the sea level (Landvik et al., 1987). The decrease in summer SST was likely the result of a general cooling, but it could also be related in part to higher thermal inertia in a more oceanic context marked by higher salinity due to lesser meltwater discharges, weak stratification and deeper thermocline. More open ocean-like conditions are coherent with the occurrence of *I. pallidum*, which is considered oligotrophic, and are compatible with the multi-proxy paleoceanographic reconstructions of northern Svalbard by Bartels et al. (2017). In our record, the sea-ice cover extent started to increase at the onset of the YD and reached a maximum at about 12.5 ka, which is almost coeval with a peak of P_BIP_{25} (Müller and Stein, 2014, Fig. 10a and b).

Although a cooling during the YD is generally assumed to have occurred at large scale in the Northern Hemisphere (e.g., Alley, 2000; Andersen et al., 2004b; see Fig. 10j), the exact timing and the regional pattern of the climate signal in the Nordic Seas and Svalbard area are not yet fully elucidated. Unlike in the Fennoscandian areas (Stroeven et al., 2016), there is no evidence that local glaciers of western (Mangerud and Landvik, 2007) and northern Svalbard (Bartels et al., 2017) experienced re-advance during the YD. ^{10}Be data even revealed that the Linnébreen glacier on west central Svalbard underwent a glacial retreat at that time (Reusche et al., 2014) whereas extensive sea-ice cover likely prevailed off eastern Svalbard, in the Storfjorden and the fjords of western Svalbard (Forwick and Vorren, 2009; Kristensen et al., 2013; Rasmussen and Thomsen, 2014). Hence, the apparent offset between southern vs. northern Fennoscandian glacier readvances during the YD can be due to particularly cold and dry climate, which limited snow accumulation and prevented glacier growth in the Svalbard area (cf. Mangerud and Landvik, 2007).

In the dinocyst assemblages of Zone II (12.6–7.6 ka), abundant *I. minutum* characterized site MSM5-712 while maximum occurrence of the cyst of *P. dalei* occurred at site PS2863 (Fig. 4). The discrepancies between the two sites are probably due to local hydrographic conditions as this interval would correspond to the development of the Arctic Coastal Front in western Svalbard and of the Polar Front in northern Svalbard, respectively. The cyst of *P. dalei* has previously been associated with the Polar Front, together with high productivity (Voronina et al., 2001; Grøsfjeld et al., 2009). *I. minutum*, which is typical for sea-ice environments and is often associated with a highly productive polynya (Hamel et al., 2002), characterizes the modern surface Arctic waters around Svalbard (Grøsfjeld et al., 2009). Therefore, from 12.6 to 7.6 ka, the study sites were probably in productive zones close to the sea-ice margin. This is compatible with the development of coastal fronts which was suggested to have occurred at 12.6 ka from the high concentration of the benthic foraminifer *Nonionellina labradorica* in cores JM02-440 and NP94-51 (see Fig. 1; Koç et al., 2002; Ślubowska et al., 2005; Ślubowska-Woldengen et al., 2007). Increased *N. labradorica* was also recorded at 12.7 ka on the northern margin of Svalbard (Bartels et al., 2017). However, from a high relative abundance of *N. labradorica*, Chauhan et al. (2014) defined the position of the Polar Front on the southern Yermak Plateau near site PS2863 significantly earlier, at 14.4–11.5 ka. The development coincides with an increase of *P. dalei* cyst numbers at site PS2863 prior to its maximum abundance during Zone II (12.6–7.6 ka). Hence, the Polar Front might have oscillated from a position close to site PS2863 northwest of Svalbard at 14.5–12.6 ka before it stabilized in a position close to the modern one (Fig. 1).

The establishment of the Arctic Coastal Front implies strengthened ESC and SCC. Their influence on the Svalbard continental shelves, which could have accounted for a cold and dry climate over Svalbard, are consistent with abundant *I. minutum*, an indicator of Arctic waters in this context, and with sedimentological evidence of other continental margin cores (Forwick and Vorren, 2009; Kristensen et al., 2013; Rasmussen and Thomsen, 2014). It is also coherent with the near-synchronous opening of the northeastern shelf of Svalbard at about 12.6 ka (Koç et al., 2002). Open waters around Svalbard necessarily fostered Arctic water circulation through the SCC and the ESC.

An increase in the strength of the EGC at about the same time, with enhanced southward flow of Arctic waters through Fram Strait, was also inferred based on low δ^{18}O in planktic foraminifers (Bauch et al., 2001; Zamelczyk et al., 2012) and the radiogenic signature in sediments from core MC16 (cf. Hillaire-Marcel et al., 2013). Regardless the precise timing of events, very important changes in sea-surface circulation of Fram Strait and around Svalbard occurred during the YD. They were likely related to a major reorganization of the ocean circulation in the Arctic and subarctic Atlantic oceans. Enhanced export of freshwater and icebergs from the Arctic Ocean (Not and Hillaire-Marcel, 2012) may have triggered the YD cooling event and the decline of AMOC strength (Tarasov and Peltier, 2005; Condron and Winsor, 2012), which occurred at about 12.7 ka (McManus et al., 2004; see Fig. 10h). In this hypothesis, the opening of the Bering Strait could well have led to enhanced southward export of sea ice through Fram Strait and to the weakening of the AMOC as simulated by Hu et al. (2015) from Community Climate System Model experiments.

6.3. The setting of "full interglacial" conditions

The Holocene has been climatically more stable than the deglaciation. However, many studies point to significant variations of sea-surface conditions on a regional scale, especially during the early Holocene which was marked by delayed establishment of optimal temperature in response to the high-latitude insolation maximum at 10 ka (e.g., Solignac et al., 2004; de Vernal and Hillaire-Marcel, 2006; Bonnet et al., 2010; Werner et al., 2011, 2013; 2016; de Vernal et al., 2013; Van Nieuwenhove et al., 2016; Zumaque et al., 2017).

In the eastern Fram Strait, our results show that the transition towards modern-like conditions occurred in surface water from the end of the YD to about 7.6 ka. It was marked by an increase in SSSs, likely in relation to the diminution of meltwater discharges after continental glaciers finally resumed. This transition was also characterized by decreasing stratification of the upper water mass, accompanied by a decreased gradient of seasonal SSTs. The recovery of the AMOC after 11.7 ka, lasting until about 8 ka, was also suggested from ^{231}Pa data (cf. McManus et al., 2004; see Fig. 10h). Intensification of the Transpolar Drift (Not and Hillaire-Marcel, 2012) together with enhanced penetration of AW into the Arctic Ocean might also have intensified turbulence in the water column, thus contributing to changes in the stratification in the Fram Strait.

In our records, there is a tenuous SST optimum in summer from 10.5 to 8.5 ka. It is characterized by low, but significant occurrences of the temperate taxa *Spiniferites mirabilis* at site MSM5-712 and *Impagidinium sphaericum* at site PS2863 (Fig. 4), which lead to reconstruct mean summer SSTs of about 2.5 °C higher than those of the late Holocene at site MSM5-712 (Fig. 6a) and minimum sea-ice cover extent at site PS2863 (Fig. 8d). In core MSM5-712, high amplitude variations in summer SSTs and salinity suggest unstable conditions possibly due to episodic freshwater supply accompanied with oscillation of the Arctic Coastal Front.

In subsurface waters, foraminifer data indicate that temperatures started to increase by about 11 ka, highlighting enhanced northward heat fluxes through the AW with maximum values reached at about 10 ka (Hald et al., 2007; Risebrobakken et al., 2011; Werner et al., 2016). However, the alkenone-based surface temperatures reached their maximum values later, between 9 and 6 ka south of Svalbard (Calvo et al., 2002; Marchal et al., 2002). The postglacial sea-surface warming generally occurred later, at about 8.5 ka in the southeastern Norwegian Sea and at various locations of the northern North Atlantic, according to diatom data (Koç and Jansen, 1992; Andersen et al., 2004a). The differences in timing of the establishment of the temperature optimum might, at least in part, be due to seasonal biases depending upon the proxy used (e.g., Sejrup et al., 2016). Nevertheless, all proxies tend to indicate that the early Holocene was marked by regionalism in the changes of ocean conditions.

The beginning of Zone I is marked by increased dinocyst concentrations at both sites, reaching maximum values at the top of the cores (Fig. 3 a, f). The concentrations are, however, lower at site

PS2863, possibly because of lower productivity due to lower nutrient inputs. An important transition in dinocyst assemblages occurred at ca. 7.6 ka when *O. centrocarpum* became dominant and the relative abundances of the main taxa reached values close to modern ones, thus leading to define Zone I (Fig. 4). The shift in dinocyst assemblages at about 8–7.5 ka, which corresponds to an abrupt decrease in *N. labyrinthus* at the benefit of *O. centrocarpum,* has been noticed in many other cores from the southern Norwegian Sea and the Fram Strait (Baumann and Matthiessen, 1992; Matthiessen and Baumann, 1997; Van Nieuwenhove et al., 2016). This change in Nordic Seas was dated slightly later, at 7.5–6 ka, and has been interpreted as being related to a major reorganization in ocean circulation (Van Nieuwenhove et al., 2016). Furthermore, the maximum $\delta^{13}C$ values in both planktic and benthic foraminifers from the deep Greenland Sea point to a setting with maximum deep-water renewal at about the same time (Bauch et al., 2001; Telesinski et al., 2014). Similarly, a transition at 7.5–6 ka, near the beginning of Zone I, is recorded in coccolith assemblages of the Nordic Seas, which also suggests an important change in the sea-surface conditions and the establishment of modern ocean properties (Baumann and Matthiessen, 1992). Finally, it is of note that *Pediastrum* is nearly absent in Zone I, which suggests limited input of freshwater.

The dinocysts of the Mid to Late Holocene interval show low amplitude variations. A cooling trend was depicted as illustrated by a decrease in winter SSTs of about 1.5 °C and an increase in sea-ice cover of 1–2 months/yr at both study sites (Fig. 9a, c). The SST decrease is coherent with the subsurface cooling recorded after 7.9 ka and 5 ka from planktic foraminifer data (Werner et al., 2013, 2016; Aagaard-Sørensen et al., 2014a). It corresponds to the establishment of the modern sea-ice factory on the East Siberian Arctic shelves (cf. Werner et al., 2013, 2016). A minor warming was however recorded during the last 3000 years in subsurface waters from Mg/Ca data (Aagaard-Sørensen et al., 2014a) and transfer functions applied to planktic foraminifer assemblages (Werner et al., 2013, 2016). Such warming could be due to limited heat loss at the surface due to stratification fostered by fresh surface waters originating from the melt of sea ice and/or icebergs. Decoupling between surface and subsurface waters would thus result from sea-ice cover increase that forced planktic foraminifers to dwell deeper in the water column into warmer waters more insulated subsurface AW in the Nordic Seas.

7. Conclusions

The dinocyst assemblages document important shifts in sea-surface conditions over the last 23,000 years at two sites in the northeastern Fram Strait. The ecological preferences of the taxa and the application of a quantitative modern analog technique permit to document seasonal SSTs, SSSs and sea-ice cover. Hence, our records provide insights into the relationship between meltwater inputs and AW inflows throughout the deglaciation, as the approach permits to disentangle salinity and temperature signals as well as the SSTs from winter and summer. Our records also reveal changes in the sea-surface circulation of northeastern Fram Strait during the deglaciation and the early Holocene.

The LGM was characterized by special hydrographic conditions in the Nordic Seas and the paleoceanographic reconstructions to date remain equivocal as they illustrate cold to relatively warm conditions depending upon the proxies used (cf. de Vernal et al., 2006). During the LGM, there was probably some AW heat advection. However, low dinocyst fluxes lead us to hypothesize that the inflows of AW to the surface might have been episodic, causing short-lived events of open waters throughout an interval otherwise characterized by generally harsh conditions. A sedimentary record of higher temporal resolution would allow to test such hypothesis.

The deglaciation started between 19 and 18 ka in the northeastern Fram Strait which remained under the influence of major meltwater discharges resulting in low salinity until about 12.6 ka. During the deglaciation, a warm episode, likely related to strong AW inflows, was recorded between 14.7 and 12.6 ka. It was interrupted by a cooling event dated of 14.5–14.1 ka at site MSM5-712 and probably related to the enhanced calving of the Barents Sea ice sheet, which can be associated with the rapid deposition of a ubiquitous fine grain sediment layer along the northwestern Barents Sea and western Svalbard continental slopes (Jessen et al., 2010; Lucchi et al., 2015). The ice surge and subsequent cooling could have been triggered by the influence of warm AW inflows. Hence, during the deglaciation the advection of heat would have led to enhanced melting of the SBSIS.

During the YD, particularly from 12.6 to 12 ka, there was a major change towards colder but more saline conditions, suggesting reduced meltwater inputs. The YD was also a transition marked by the onset of coastal fronts at the western and northern margins of Svalbard as the result of enhanced contribution of Arctic waters. The transition towards full interglacial conditions was marked by increasing salinity until modern like values were reached at about 7.6 ka. During the Mid to Late Holocene, a general cooling trend was detected mostly from a decrease in winter SSTs.

Our study combining SST and SSS reconstructions permitted to identify important climate-related parameters like meltwater discharges and stratification of the surface water layer. The major transitions in sea-surface conditions, notably those which occurred shortly after the onset of the BA and the YD, seem closely related to shifts in the AMOC strength as reconstructed from mid latitude North Atlantic geochemical data (e.g., McManus et al., 2004; see Fig. 10). This relation points to high sensitivity of eastern Fram Strait to AW inflow intensity and its critical role in ocean circulation.

Acknowledgements

This study was supported by the *Fonds de recherche du Québec Nature et technologies* (FRQNT) to JF through scholarship and to GEOTOP Research Center through the Strategic Clusters program, the Natural Sciences and Engineering Research Council (NSERC) of Canada through discovery grant to AdV (38340) and the NSERC-CREATE grant to ArcTrain (432295), and the Academy of Sciences, Humanities and Literature Mainz through the *Akademienprogramm*. The laboratory analyses have been made in the micropaleontology and laboratory of GEOTOP at UQAM. The sediment samples from cores PS2863-1 and PS2832-2BC were made available through the ARK-XIII/2 expedition of the *RV Polarstern* and through the MSM05/5b expedition of the *RV Maria S. Merian* for core MSM5/5-712-2. A ^{14}C age was operated by the NOSAMS facility at the Woods Hole Oceanographic Institution with National Science Foundation sponsorship (OCE-1239667). Special thanks go to Maryse Henry and Sophie Bonnet for the palynological analysis of the first 315 cm of the MSM5/5-712-2 core. We thank Simon Van Bellen for his help in developing the age models from the Bacon software. We are grateful to the three anonymous reviewers of the journal for their critical comments on the original manuscript.

References

Aagaard-Sørensen, S., Husum, K., Hald, M., Marchitto, T., Godtliebsen, F., 2014a. Sub sea surface temperatures in the Polar North Atlantic during the Holocene: planktic foraminiferal Mg/Ca temperature reconstructions. Holocene 24, 93–103.

Aagaard-Sørensen, S., Husum, K., Werner, K., Spielhagen, R.F., Hald, M., Marchitto, T.M., 2014b. A late glacial–early Holocene multiproxy record from the eastern Fram Strait, polar North Atlantic. Mar. Geol. 355, 15–26.

Allan, E., de Vernal, A., Knudsen, Hillaire-Marcel, C., Moros, M., Ribeiro, S., Ouellet-Bernier, M.-M., Seidenkrantz, M.-S., 2018. Late Holocene sea surface instabilities in the Disko Bugt area, West Greenland, in phase with $\delta^{18}O$ oscillations at Camp Century. Paleoceanography Paleoclimatology 33, 227–243.
Alley, R.B., 2000. The Younger Dryas cold interval as viewed from central Greenland. Quat. Sci. Rev. 19, 213–226.
Andersen, E.S., Dokken, T.M., Elverhøi, A., Solheim, A., Fossen, I., 1996. Late Quaternary sedimentation and glacial history of the western Svalbard continental margin. Mar. Geol. 133, 123–156.
Andersen, C., Koç, N., Moros, M., 2004a. A highly unstable Holocene climate in the subpolar North Atlantic: evidence from diatoms. Quat. Sci. Rev. 23, 2155–2166.
Andersen, K.K., Azuma, N., Barnola, J.-M., Bigler, M., Biscaye, P., Caillon, N., Chappellaz, J., Clausen, H.B., Dahl-Jensen, D., Fischer, H., 2004b. High-resolution record of Northern Hemisphere climate extending into the last interglacial period. Nature 431, 147–151.
Bartels, M., Titschack, J., Fahl, K., Stein, R., Seidenkrantz, M.-S., Hillaire-Marcel, C., Hebbeln, D., 2017. Atlantic Water advection vs. glacier dynamics in northern Spitsbergen since early deglaciation. Clim. Past 13, 1717.
Bauch, H.A., Erlenkeuser, H., Spielhagen, R.F., Struck, U., Matthiessen, J., Thiede, J., Heinemeier, J., 2001. A multiproxy reconstruction of the evolution of deep and surface waters in the subarctic Nordic seas over the last 30,000 yr. Quat. Sci. Rev. 20, 659–678.
Baumann, K.-H., Matthiessen, J., 1992. Variations in surface water mass conditions in the Norwegian Sea: evidence from Holocene coccolith and dinoflagellate cyst assemblages. Mar. Micropaleontol. 20, 129–146.
Blaauw, M., Christen, J.A., 2011. Flexible paleoclimate age-depth models using an autoregressive gamma process. Bayesian Analysis 6, 457–474.
Bond, G., Broecker, W., Johnsen, S., McManus, J., Labeyrie, L., Jouzel, J., Bonani, G., 1993. Correlations between climate records from North Atlantic sediments and Greenland ice. Nature 365, 143–147.
Bonnet, S., de Vernal, A., Hillaire-Marcel, C., Radi, T., Husum, K., 2010. Variability of sea-surface temperature and sea-ice cover in the Fram Strait over the last two millennia. Mar. Micropaleontol. 74, 59–74.
Budéus, G., 2007. Short Cruise Report RV Maria S. Merian Cruise MSM05/5. University of Hamburg, Institute of Oceanography.
Calvo, E., Grimalt, J., Jansen, E., 2002. High resolution U 37 K sea surface temperature reconstruction in the Norwegian Sea during the Holocene. Quat. Sci. Rev. 21, 1385–1394.
Chauhan, T., Rasmussen, T., Noormets, R., Jakobsson, M., Hogan, K., 2014. Glacial history and paleoceanography of the southern Yermak Plateau since 132 ka BP. Quat. Sci. Rev. 92, 155–169.
Chauhan, T., Rasmussen, T.L., Noormets, R., 2016. Palaeoceanography of the Barents Sea continental margin, north of Nordaustlandet, Svalbard, during the last 74 ka. Boreas 45, 76–99.
Condron, A., Winsor, P., 2012. Meltwater routing and the younger Dryas. Proc. Natl. Acad. Sci. Unit. States Am. 109, 19928–19933.
Conkright, M.E., Locarnini, R.A., Garcia, H.E., O'Brien, T.D., Boyer, T.P., Stephens, C., Antonov, J.I., 2002. World Ocean Atlas 2001: Objective Analyses, Data Statistics, and Figures: CD-rom Documentation. US Department of Commerce, National Oceanic and Atmospheric Administration, National Oceanographic Data Center, Ocean Climate Laboratory.
Consolaro, C., Rasmussen, T.L., Panieri, G., 2018. Palaeoceanographic and environmental changes in the eastern Fram Strait during the last 14,000 years based on benthic and planktonic foraminifera. Mar. Micropaleontol. 139, 84–101.
Cronin, T.M., Dwyer, G.S., Farmer, J., Bauch, H.A., Spielhagen, R.F., Jakobsson, M., Nilsson, J., Briggs Jr., W., Stepanova, A., 2012. Deep Arctic Ocean warming during the last glacial cycle. Nat. Geosci. 5, 631–634.
de Vernal, A., Bilodeau, G., Hillaire-Marcel, C., Kassou, N., 1992. Quantitative assessment of carbonate dissolution in marine sediments from foraminifer linings vs. shell ratios: davis Strait, northwest North Atlantic. Geology 20, 527–530.
de Vernal, A., Hillaire-Marcel, C., Turon, J., Matthiessen, J., Rochon, A., Vallières, S., Levesque, L., 2000. Sea-surface conditions in middle to high latitudes of the North Atlantic during the last glacial maximum (LGM): the cold paradigm revisited. Can. J. Earth Sci. 37, 725–750.
de Vernal, A., Henry, M., Matthiessen, J., Mudie, P.J., Rochon, A., Boessenkool, K.P., Eynaud, F., Grøsfjeld, K., Guiot, J., Hamel, D., Harland, R., Head, M.J., Kunz-Pirrung, M., Levac, E., Loucheur, V., Peyron, O., Pospelova, V., Radi, T., Turon, J.-L., Voronina, E., 2001. Dinoflagellate cyst assemblages as tracers of sea-surface conditions in the northern North Atlantic, Arctic and sub-Arctic seas: the new 'n= 677' data base and its application for quantitative palaeoceanographic reconstruction. J. Quat. Sci. 16, 681–698.
de Vernal, A., Eynaud, F., Henry, M., Hillaire-Marcel, C., Londeix, L., Mangin, S., Matthiessen, J., Marret, F., Radi, T., Rochon, A., Solignac, S., Turon, J.L., 2005. Reconstruction of sea-surface conditions at middle to high latitudes of the Northern Hemisphere during the Last Glacial Maximum (LGM) based on dinoflagellate cyst assemblages. Quat. Sci. Rev. 24, 897–924.
de Vernal, A., Hillaire-Marcel, C., 2006. Provincialism in trends and high frequency changes in the northwest North Atlantic during the Holocene. Global Planet. Change 54, 263–290.
de Vernal, A., Rosell-Melé, A., Kucera, M., Hillaire-Marcel, C., Eynaud, F., Weinelt, M., Dokken, T., Kageyama, M., 2006. Comparing proxies for the reconstruction of LGM sea-surface conditions in the northern North Atlantic. Quat. Sci. Rev. 25, 2820–2834.
de Vernal, A., Bilodeau, G., Henry, M., 2010. Micropaleontological Preparation Techniques and Analyses. Cahier du Geotop.
de Vernal, A., Hillaire-Marcel, C., Rochon, A., Fréchette, B., Henry, M., Solignac, S., Bonnet, S., 2013. Dinocyst-based reconstructions of sea ice cover concentration during the Holocene in the Arctic Ocean, the northern North Atlantic Ocean and its adjacent seas. Quat. Sci. Rev. 79, 111–121.
Dodge, J., 1989. Some revisions of the family Gonyaulacaceae (Dinophyceae) based on a scanning electron microscope study. Bot. Mar. 32, 275–298.
Dokken, T.M., Jansen, E., 1999. Rapid changes in the mechanism of ocean convection during the last glacial period. Nature 401, 458–461.
Ellegaard, M., 2000. Variations in dinoflagellate cyst morphology under conditions of changing salinity during the last 2000 years in the Limfjord, Denmark. Rev. Palaeobot. Palynol. 109, 65–81.
Eynaud, F., Duprat, J., Turon, J.-L., Zaragosi, S., 2004. Paleohydrological evidence of a two step evolution of the Last Glacial Maximum (LGM) along the western European margins. In: Eigth International Conference on Paleoceanography, Biarritz, September, Programme and Abstracts. B1–153.
Fahrbach, E., Meincke, J., Østerhus, S., Rohardt, G., Schauer, U., Tverberg, V., Verduin, J., 2001. Direct measurements of volume transports through Fram Strait. Polar Res. 20, 217–224.
Falardeau, J., 2017. Paléocéanographie du nord-est du Détroit de Fram depuis le dernier maximum glaciaire. M.Sc. dissertation. Université du Québec à Montréal.
Fetterer, F., Knowles, K., Meier, W., Savoie, M., 2016. Sea Ice Index, Version 2. National Snow and Ice Data Center, Boulder, CO, USA (Digital Media, updated daily).
Forwick, M., Vorren, T.O., 2009. Late Weichselian and Holocene sedimentary environments and ice rafting in isfjorden, spitsbergen. Palaeogeogr. Palaeoclimatol. Palaeoecol. 280, 258–274.
Gascard, J.-C., Richez, C., Rouault, C., 1995. New insights on large-scale oceanography in Fram Strait. The West Spitsbergen Current 49, 131–182.
Gibb, O.T., Hillaire-Marcel, C., de Vernal, A., 2014. Oceanographic regimes in the northwest Labrador Sea since Marine Isotope Stage 3 based on dinocyst and stable isotope proxy records. Quat. Sci. Rev. 92, 269–279.
Giraudeau, J., (in preparation). EPOC (University Bordeaux 1/CNRS) within the Framework of an Ongoing IFM-geomar. EPOC collaboration.
Grøsfjeld, K., Harland, R., Howe, J., 2009. Dinoflagellate cyst assemblages inshore and offshore Svalbard reflecting their modern hydrography and climate. Norw. J. Geol. 89, 121–134.
Guiot, J., 1990. Methodology of the last climatic cycle reconstruction in France from pollen data. Palaeogeography, Palaeoclimatology, Palaeoelogy 80, 49–69.
Guiot, J., de Vernal, A., 2011. Is spatial autocorrelation introducing biases in the apparent accuracy of paleoclimatic reconstructions? Quat. Sci. Rev. 30, 1965–1972.
Hald, M., Dokken, T., Mikalsen, G., 2001. Abrupt climatic change during the last interglacial–glacial cycle in the polar North Atlantic. Mar. Geol. 176, 121–137.
Hald, M., Andersson, C., Ebbesen, H., Jansen, E., Klitgaard-Kristensen, D., Risebrobakken, B., Salomonsen, G.R., Sarnthein, M., Sejrup, H.P., Telford, R.J., 2007. Variations in temperature and extent of atlantic water in the northern North atlantic during the Holocene. Quat. Sci. Rev. 26, 3423–3440.
Hall, I.R., Moran, S., Zahn, R., Knutz, P.C., Shen, C.C., Edwards, R., 2006. Accelerated drawdown of meridional overturning in the late-glacial Atlantic triggered by transient pre-H event freshwater perturbation. Geophys. Res. Lett. 33.
Hamel, D., de Vernal, A., Gosselin, M., Hillaire-Marcel, C., 2002. Organic-walled microfossils and geochemical tracers: sedimentary indicators of productivity changes in the North Water and northern Baffin Bay during the last centuries. Deep Sea Res. Part II Top. Stud. Oceanogr. 49, 5277–5295.
Hebbeln, D., Dokken, T., Andersen, E.S., Hald, M., Elverhøi, A., 1994. Moisture Supply for Northern Ice-sheet Growth during the Last Glacial Maximum.
Hebbeln, D., Wefer, G., 1997. Late quaternary paleoceanography in the Fram Strait. Paleoceanography 12, 65–78.
Heinrich, H., 1988. Origin and consequences of cyclic ice rafting in the Northeast Atlantic Ocean during the past 130,000 years. Quat. Res. (Duluth) 29, 142–152.
Hemming, S.R., 2004. Heinrich events: massive late Pleistocene detritus layers of the North Atlantic and their global climate imprint. Rev. Geophys. 42, RG1005.
Hillaire-Marcel, C., Maccali, J., Not, C., Poirier, A., 2013. Geochemical and isotopic tracers of Arctic sea ice sources and export with special attention to the Younger Dryas interval. Quat. Sci. Rev. 79, 184–190.
Hu, A., Meehl, G.A., Han, W., Otto-Bliestner, B., Abe-Ouchi, A., Rosenbloom, N., 2015. Effects of the Bering Strait closure on AMOC and global climate under different background climates. Prog. Oceanogr. 132, 174–196.
Hughes, A.L., Gyllencreutz, R., Lohne, Ø.S., Mangerud, J., Svendsen, J.I., 2016. The last Eurasian ice sheets–a chronological database and time-slice reconstruction, DATED-1. Boreas 45, 1–45.
Ivanovic, R., Grégoire, L., Wickert, A., Burke, A., Valdes, P., 2017. Heinrich Stadial 1 Caused by Acceleration of Eurasian Deglaciation ~18.5 Ka, Abstract Goldschmidt 2017.
Jessen, S.P., Rasmussen, T.L., Nielsen, T., Solheim, A., 2010. A new Late Weichselian and Holocene marine chronology for the western Svalbard slope 30,000–0 cal years BP. Quat. Sci. Rev. 29, 1301–1312.
Jones, G.A., Keigwin, L.D., 1988. Evidence from Fram Strait (78 N) for early deglaciation. Nature 336, 56–59.
Jorissen, F.J., Fontanier, C., Thomas, E., 2007. Chapter seven paleoceanographical proxies based on deep-sea benthic foraminiferal assemblage characteristics. Developments in Marine Geology 1, 263–325.
Koç, N., Jansen, E., 1992. A high-resolution diatom record of the last deglaciation

from the SE Norwegian Sea: documentation of rapid climatic changes. Paleoceanography 7, 499–520.
Koç, N., Klitgaard-Kristensen, D., Hasle, K., Forsberg, C.F., Solheim, A., 2002. Late glacial palaeoceanography of hinlopen strait, northern svalbard. Polar Res. 21, 307–314.
Kodrans-Nsiah, M., de Lange, G.J., Zonneveld, K.A.F., 2008. A natural exposure experiment on short-term species-selective aerobic degradation of dinoflagellate cysts. Rev. Palaeobot. Palynol. 152, 32–39.
Kucera, M., Rosell-Melé, A., Schneider, R., Waelbroeck, C., Weinelt, M., 2005. Multiproxy approach for the reconstruction of the glacial ocean surface (MARGO). Quat. Sci. Rev. 24, 813–819.
Kristensen, D.K., Rasmussen, T.L., Koç, N., 2013. Palaeoceanographic changes in the northern Barents Sea during the last 16 000 years—new constraints on the last deglaciation of the Svalbard–Barents Sea ice sheet. Boreas 42, 798–813.
Landvik, J.Y., Mangerud, J., Salvigsen, O., 1987. The Late Weichselian and Holocene shoreline displacement on the west-central coast of Svalbard. Polar Res. 5, 29–44.
Landvik, J.Y., Bondevik, S., Elverhøi, A., Fjeldskaar, W., Mangerud, J., Salvigsen, O., Siegert, M.J., Svendsen, J.-I., Vorren, T.O., 1998. The last glacial maximum of Svalbard and the Barents Sea area: ice sheet extent and configuration. Quat. Sci. Rev. 17, 43–75.
Leduc, J., 2001. Study of Benthic Foraminiferal Populations in the Sediments of the Saguenay Fjord. M.Sc. dissertation. Université du Québec à Montréal.
Lehman, S., Jones, G., Keigwin, L., Andersen, E., Butenkoi, G., Østmo, S., 1991. Initiation of Fennoscandian Ice-sheet Retreat during the Last Deglaciation.
Levine, R.C., Bigg, G.R., 2008. Sensitivity of the glacial ocean to Heinrich events from different iceberg sources, as modeled by a coupled atmosphere-iceberg-ocean model. Paleoceanography 23.
Loeng, H., 1991. Features of the physical oceanographic conditions of the Barents Sea. Polar Res. 10, 5–18.
Lucchi, R.G., Sagnotti, L., Camerlenghi, A., Macrì, P., Rebesco, M., Pedrosa, M.T., Giorgetti, G., 2015. Marine sedimentary record of meltwater pulse 1a along the NW Barents Sea continental margin. arktos 1, 7.
Mangerud, J., 1972. Radiocarbon dating of marine shells, including a discussion of apparent age of recent shells from Norway. Boreas 1, 143–172.
Mangerud, J., Gulliksen, S., 1975. Apparent radiocarbon ages of recent marine shells from Norway, Spitsbergen, and Arctic Canada. Quat. Res. (Duluth) 5, 263–273.
Mangerud, J., Landvik, J.Y., 2007. Younger Dryas cirque glaciers in western spitsbergen: smaller than during the little ice age. Boreas 36, 278–285.
Manley, T., 1995. Branching of atlantic water within the Greenland-Spitsbergen passage: an estimate of recirculation. J. Geophys. Res.: Oceans 100, 20627–20634.
Marchal, O., Cacho, I., Stocker, T.F., Grimalt, J.O., Calvo, E., Martrat, B., Shackleton, N., Vautravers, M., Cortijo, E., et van Kreveld, S., 2002. Apparent long-term cooling of the sea surface in the northeast Atlantic and Mediterranean during the Holocene. Quat. Sci. Rev. 21 (4), 455–483.
Marret, F., Zonneveld, K.A., 2003. Atlas of modern organic-walled dinoflagellate cyst distribution. Rev. Palaeobot. Palynol. 125, 1–200.
Maslowski, W., Marble, D., Walczowski, W., Schauer, U., Clement, J.L., Semtner, A.J., 2004. On climatological mass, heat, and salt transports through the Barents Sea and Fram Strait from a pan-Arctic coupled ice-ocean model simulation. J. Geophys. Res.: Oceans 109.
Matthews, J., 1969. The assessment of a method for the determination of absolute pollen frequencies. New Phytol. 68, 161–166.
Matthiessen, J., 1995. Distribution patterns of dinoflagellate cysts and other organic-walled microfossils in recent Norwegian-Greenland Sea sediments. Mar. Micropaleontol. 24, 307–334.
Matthiessen, J., Baumann, A., 1997. Dinoflagellate cyst records from the East Greenland continental margin during the last 15,000 years: implications for paleoceanographic reconstructions. In: Hass, H.C., Kaminski, M.A. (Eds.), Contributions to the Micropaleontology and Paleoceanography of the Northern North Atlantic. Gryzbowski Foundation Special Publication, pp. 149–165.
McManus, J.F., Francois, R., Gherardi, J.-M., Keigwin, L.D., Brown-Leger, S., 2004. Collapse and rapid resumption of Atlantic meridional circulation linked to deglacial climate changes. Nature 428, 834–837.
Mertens, K.N., Bringué, M., Van Nieuwenhove, N., Takano, Y., Pospelova, V., Rochon, A., De Vernal, A., Radi, T., Dale, B., Patterson, R.T., Weckström, K., Andrén, E., Louwye, S., Matsuoka, K., 2012. Process length variation of the cyst of the dinoflagellate *Protoceratium reticulatum* in the North Pacific and Baltic-Skagerrak region: calibration as an annual density proxy and first evidence of pseudo-cryptic speciation. J. Quat. Sci. 27, 734–744.
Müller, J., Werner, K., Stein, R., Fahl, K., Moros, M., Jansen, E., 2012. Holocene cooling culminates in sea ice oscillations in Fram Strait. Quat. Sci. Rev. 47, 1–14.
Müller, J., Stein, R., 2014. High-resolution record of late glacial and deglacial sea ice changes in Fram Strait corroborates ice–ocean interactions during abrupt climate shifts. Earth Planet Sci. Lett. 403, 446–455.
National Snow and Ice Data Center (NSIDC), 2003. Brightness Temperature and Ice Concentrations Grids for the Polar Regions. NSIDC Distributed Active Archive Center, Boulder, CO.
Nørgaard-Pedersen, N., Spielhagen, R.F., Erlenkeuser, H., Grootes, P.M., Heinemeier, J., Knies, J., 2003. Arctic Ocean during the Last Glacial Maximum: Atlantic and polar domains of surface water mass distribution and ice cover. Paleoceanography 18 (3), 1063.
Not, C., Hillaire-Marcel, C., 2012. enhanced sea-ice export from the arctic during the younger Dryas. Nat. Commun. 3, 647.
Olsson, I.U., 1980. Content of 14 C in marine mammals from northern Europe. Radiocarbon 22, 662–675.
Pflaumann, U., Sarnthein, M., Chapman, M., d'Abreu, L., Funnell, B., Huels, M., Kiefer, T., Maslin, M., Schulz, H., Swallow, J., van Kreveld, S., Vautravers, M., Vogelsang, E., Weinelt, M., 2003. Glacial North Atlantic: sea-surface conditions reconstructed by GLAMAP 2000. Paleoceanography 18 (3), 1065.
Rasmussen, S.O., Andersen, K.K., Svensson, A.M., Steffensen, J.P., Vinther, B.M., Clausen, H.B., Siggaard-Andersen, M.L., Johnsen, S.J., Larsen, L.B., Dahl-Jensen, D., Bigler, M., Röthlisberger, R., Fischer, H., Goto-Azuma, K., Hansson, M.E., Ruth, U., 2006. A new Greenland ice core chronology for the last glacial termination. J. Geophys. Res. 111.
Rasmussen, T.L., Thomsen, E., Ślubowska, M.A., Jessen, S., Solheim, A., Koç, N., 2007. Paleoceanographic evolution of the SW Svalbard margin (76°N) since 20,000 14C yr BP. Quat. Res. (Duluth) 67, 100–114.
Rasmussen, T.L., Thomsen, E., 2008. Warm Atlantic surface water inflow to the Nordic seas 34–10 calibrated ka BP. Paleoceanography 23.
Rasmussen, T.L., Forwick, M., Mackensen, A., 2012. Reconstruction of inflow of atlantic water to isfjorden, svalbard during the Holocene: correlation to climate and seasonality. Mar. Micropaleontol. 94–95, 80–90.
Rasmussen, T., Thomsen, E., 2014. Brine formation in relation to climate changes and ice retreat during the last 15,000 years in Storfjorden, Svalbard, 76–78°N. Paleoceanography 29, 911–929.
Reimer, P.J., Bard, E., Bayliss, A., Beck, J.W., Blackwell, P.G., Bronk Ramsey, C., Buck, C.E., Cheng, H., Edwards, R.L., Friedrich, M., 2013. IntCal13 and Marine13 Radiocarbon Age Calibration Curves 0-50,000 Years Cal BP.
Reusche, M., Winsor, K., Carlson, A.E., Marcott, S.A., Rood, D.H., Novak, A., Roof, S., Retelle, M., Werner, A., Caffee, M., 2014. 10 Be surface exposure ages on the late-Pleistocene and Holocene history of Linnébreen on Svalbard. Quat. Sci. Rev. 89, 5–12.
Risebrobakken, B., Dokken, T., Smedsrud, L.H., Andersson, C., Jansen, E., Moros, M., Ivanova, E.V., 2011. Early Holocene temperature variability in the Nordic Seas: the role of oceanic heat advection versus changes in orbital forcing. Paleoceanography 26.
Rochon, A., Vernal, A.D., Turon, J.-L., Matthiessen, J., Head, M., 1999. Distribution of recent dinoflagellate cysts in surface sediments from the North Atlantic Ocean and adjacent seas in relation to sea-surface parameters. Am. Assoc. Stratigr. Palynol. Contrib. Ser. 35, 1–146.
Rochon, A., Mudie, P.J., Aksu, A.E., Gillespie, H., 2002. Pterocystagen. nov.: a new dinoflagellate cyst from pleistocene glacial-stage sediments of the black and Marmara Seas. Palynology 26, 95–105.
Rochon, A., Lewis, J., Ellegaard, M., Harding, I.C., 2009. The Gonyaulax spinifera (Dinophyceae) "complex": perpetuating the paradox? Rev. Palaeobot. Palynol. 155, 52–60.
Rørvik, K.L., Rasmussen, T.L., Hald, M., Husum, K., 2013. Intermediate water ventilation in the Nordic seas during MIS 2. Geophys. Res. Lett. 40, 1805–1810.
Rosell-Melé, A., Comes, P., 1999. Evidence for a Warm Last Glacial Maximum in the Nordic Seas or an example of shortcomings in UK37′and UK37to estimate low sea surface temperature? Paleoceanography 14, 770–776.
Rudels, B., Friedrich, H.J., Quadfasel, D., 1999. The Arctic circumpolar boundary current. Deep Sea Research Part II. Topical Studies in Oceanography 46, 1023–1062.
Rudels, B., Meyer, R., Fahrbach, E., Ivanov, V., Østerhus, S., Quadfasel, D., Schauer, U., Tverberg, V., Woodgate, R., 2000. Water Mass Distribution in Fram Strait and over the Yermak Plateau in Summer 1997, Annales Geophysicae. Springer, pp. 687–705.
Rudels, B., Björk, G., Nilsson, J., Winsor, P., Lake, I., Nohr, C., 2005. The interaction between waters from the Arctic ocean and the nordic seas north of Fram Strait and along the east Greenland current: results from the Arctic ocean-02 oden expedition. J. Mar. Syst. 55, 1–30.
Sarnthein, M., Jansen, E., Weinelt, M., Arnold, M., Duplessy, J.C., Erlenkeuser, H., Flatøy, A., Johannessen, G., Johannessen, T., Jung, S., 1995. Variations in Atlantic surface ocean paleoceanography, 50°-80° N: a time-slice record of the last 30,000 years. Paleoceanography 10, 1063–1094.
Sarnthein, M., Pflaumann, U., Weinelt, M., 2003. Past extent of sea ice in the northern North Atlantic inferred from foraminiferal paleotemperature estimates. Paleoceanography 18 (2), 1047.
Schauer, U., 2004. Arctic warming through the Fram Strait: oceanic heat transport from 3 years of measurements. J. Geophys. Res. 109.
Schauer, U., Beszczynska-Möller, A., Walczowski, W., Fahrbach, E., Piechura, J., Hansen, E., 2008. Variation of Measured Heat Flow through the Fram Strait between 1997 and 2006, Arctic–subarctic Ocean Fluxes. Springer, pp. 65–85.
Sejrup, H.P., Seppä, H., McKay, N.P., Kaufman, D.S., Geirsdóttir, Á., de Vernal, A., Renssen, H., Husum, K., Jennings, A., Andrews, J.T., 2016. North Atlantic-Fennoscandian Holocene climate trends and mechanisms. Quat. Sci. Rev. 147, 365–378.
Skogseth, R., Haugan, P.M., Jakobsson, M., 2005. Watermass transformations in storfjorden. Continent. Shelf Res. 25, 667–695.
Ślubowska, M.A., Koç, N., Rasmussen, T.L., Klitgaard-Kristensen, D., 2005. Changes in the flow of Atlantic water into the Arctic Ocean since the last deglaciation: evidence from the northern Svalbard continental margin, 80°N. Paleoceanography 20, PA4014.
Ślubowska-Woldengen, M., Rasmussen, T.L., Koç, N., Klitgaard-Kristensen, D., Nilsen, F., Solheim, A., 2007. Advection of Atlantic Water to the western and northern Svalbard shelf since 17,500 cal. yr BP. Quat. Sci. Rev. 26, 463–478.
Ślubowska-Woldengen, M., Koç, N., Rasmussen, T.L., Klitgaard-Kristensen, D.,

Hald, M., Jennings, A.E., 2008. Time-slice reconstructions of ocean circulation changes on the continental shelf in the Nordic and Barents Seas during the last 16,000 cal. yr BP. Quat. Sci. Rev. 27, 1476–1492.
Solignac, S., de Vernal, A., Hillaire-Marcel, C., 2004. Holocene sea-surface conditions in the North Atlantic—contrasted trends and regimes in the western and eastern sectors (Labrador Sea vs. Iceland Basin). Quat. Sci. Rev. 23, 319–334.
Spielhagen, R.F., Werner, K., Sørensen, S.A., Zamelczyk, K., Kandiano, E., Budeus, G., Husum, K., Marchitto, T.M., Hald, M., 2011. Enhanced modern heat transfer to the Arctic by warm Atlantic water. Science 331, 450–453.
Spielhagen, R.F., Müller, J., Wagner, A., Werner, K., Lohmann, G., Prange, M., Stein, R., 2014. Holocene environmental variability in the arctic gateway. In: Schulz, M., Paul, A. (Eds.), Integrated Analysis of Interglacial Climate Dynamics, Springer Briefs. Springer-Verlag, Berlin, pp. 37–41.
Stanford, J., Rohling, E.J., Bacon, S., Roberts, A., Grousset, F., Bolshaw, M., 2011. A new concept for the paleoceanographic evolution of Heinrich event 1 in the North Atlantic. Quat. Sci. Rev. 30, 1047–1066.
Stein, R., Fahl, K., 1997. Scientific cruise report of the Arctic expedition ARK-XIII/2 of RV" Polarstern" in 1997= Wissenschaftlicher Fahrtbericht über die Arktis-Expedition ARK-XIII/2 von 1997 mit FS" Polarstern". Berichte zur Polarforschung (Reports on Polar Research) 255.
Stern, J.V., Lisiecki, L.E., 2014. Termination 1 timing in radiocarbon dated regional benthic δ18O stacks. Paleoceanography 29, 1127–1142.
Stockmarr, J., 1971. Tablets with spores used in absolute pollen analysis. Pollen Spores 13, 615–621.
Streel, M., Bless, M., 1980. Occurrence and significance of reworked palynomorphs. Meded. Rijks Geol. Dienst 32, 69–80.
Stroeven, A.P., Hättestrand, C., Kleman, J., Heyman, J., Fabel, D., Fredin, O., Goodfellow, B.W., Harbor, J.M., Jansen, J.D., Olsen, L., 2016. Deglaciation of fennoscandia. Quat. Sci. Rev. 147, 91–121.
Tarasov, L., Peltier, W.R., 2005. Arctic freshwater forcing of the Younger Dryas cold reversal. Nature 435, 662–665.
Telford, R.J., 2006. Limitations of dinoflagellate cyst transfer functions. Quat. Sci. Rev. 25, 1375–1382.
Telford, R., Birks, H., 2009. Evaluation of transfer functions in spatially structured environments. Quat. Sci. Rev. 28, 1309–1316.
Telesinski, M.M., Spielhagen, R.F., Bauch, H.A., 2014. Water mass evolution of the Greenland Sea since lateglacial times. Clim. Past 10, 123–136.
Van Nieuwenhove, N., Baumann, A., Matthiessen, J., Bonnet, S., de Vernal, A., 2016. Sea surface conditions in the southern Nordic Seas during the Holocene based on dinoflagellate cyst assemblages. Holocene 26, 722–735.
Voronina, E., Polyak, L., Vernal, A.D., Peyron, O., 2001. Holocene variations of sea-surface conditions in the southeastern Barents Sea, reconstructed from dinoflagellate cyst assemblages. J. Quat. Sci. 16, 717–726.
Walczowski, W., Piechura, J., Osinski, R., Wieczorek, P., 2005. The West Spitsbergen Current volume and heat transport from synoptic observations in summer. Deep Sea Research Part I. Oceanographic Research Papers 52, 1374–1391.
Walczowski, W., Piechura, J., 2007. Pathways of the Greenland sea warming. Geophys. Res. Lett. 34.
Walker, M.J.C., Berkelhammer, M., Björck, S., Cwynar, L.C., Fisher, D.A., Long, A.J., Lowe, J.J., Newnham, R.M., Rasmussen, S.O., Weiss, H., 2012. Formal subdivision of the Holocene series/epoch: a discussion paper by a working group of INTIMATE (integration of ice-core, marine and terrestrial records) and the subcommission on quaternary stratigraphy (international commission on stratigraphy). J. Quat. Sci. 27, 649–659.
Weinelt, M., Sarnthein, M., Pflaumann, U., Schulz, H., Jung, S., Erlenkeuser, H., 1996. Ice-free Nordic seas during the last glacial maximum. Potential sites of deep-water formation. Paleoclimates 1, 283–309.
Weinelt, M., Vogelsang, E., Kucera, M., Pflaumann, U., Sarnthein, M., Voelker, A., Erlenkeuser, H., Malmgren, B.A., 2003. Variability of north atlantic heat transfer during MIS 2. Paleoceanography 18 (3), 1071.
Werner, K., Spielhagen, R.F., Bauch, D., Hass, H.C., Kandiano, E., Zamelczyk, K., 2011. Atlantic water advection to the eastern Fram Strait — multiproxy evidence for late Holocene variability. Palaeogeogr. Palaeoclimatol. Palaeoecol. 308, 264–276.
Werner, K., Spielhagen, R.F., Bauch, D., Hass, H.C., Kandiano, E., 2013. Atlantic Water advection versus sea-ice advances in the eastern Fram Strait during the last 9 ka: multiproxy evidence for a two-phase Holocene. Paleoceanography 28, 283–295.
Werner, K., Müller, J., Husum, K., Spielhagen, R.F., Kandiano, E.S., Polyak, L., 2016. Holocene sea subsurface and surface water masses in the Fram Strait – comparisons of temperature and sea-ice reconstructions. Quat. Sci. Rev. 147, 194–209. https://doi.org/10.1016/j.quascirev.2015.09.007.
Williams, G.L., Brideaux, W.W., 1975. Palynologic Analyses of Upper Mesozoic and Cenozoic Rocks of the Grand Banks, Atlantic continental Margin. Department of Energy, Mines and Resources available from: Information Canada).
Xiao, X., Fahl, K., Müller, J., Stein, R., 2015. Sea-ice distribution in the modern Arctic Ocean: biomarker records from trans-Arctic Ocean surface sediments. Geochem. Cosmochim. Acta 155, 16–29.
Zamelczyk, K., Rasmussen, T.L., Husum, K., Haflidason, H., de Vernal, A., Ravna, E.K., Hald, M., Hillaire-Marcel, C., 2012. Paleoceanographic changes and calcium carbonate dissolution in the central Fram Strait during the last 20ka. Quat. Res. (Duluth) 78, 405–416.
Zamelczyk, K., Rasmussen, T.L., Husum, K., Godtliebsen, F., Hald, M., 2014. Surface water conditions and calcium carbonate preservation in the Fram Strait during marine isotope stage 2, 28.8-15.4 kyr. Paleoceanography 29, 1–12.
Zumaque, J., Eynaud, F., de Vernal, A., 2017. Holocene paleoceanography of the Bay of Biscay: evidence for west-east linkages in the North Atlantic based on dinocyst data. Palaeogeogr. Palaeoclimatol. Palaeoecol. 468, 403–413.